

THE SECULAR EVOLUTION OF DISK STRUCTURAL PARAMETERS

VICTOR P. DEBATTISTA,^{1,2} LUCIO MAYER, AND C. MARCELLA CAROLLO

Institut für Astronomie, ETH Zürich, Scheuchzerstrasse 7, CH-8093 Zürich, Switzerland; lucio@phys.ethz.ch, marcella.carollo@phys.ethz.ch

BEN MOORE

Department of Theoretical Physics, University of Zürich, Winterthurerstrasse 190, CH-8057 Zürich, Switzerland; moore@physik.unizh.ch

JAMES WADSLEY

Department of Physics and Astronomy, McMaster University, 1280 Main Street West, Hamilton, ON L8S 4M1, Canada;
wadsley@mcmaster.ca

AND

THOMAS QUINN

Astronomy Department, University of Washington, Box 351580, Seattle, WA 98195; trq@astro.washington.edu

Received 2005 August 26; accepted 2006 March 5

ABSTRACT

We present a comprehensive series of simulations to study the secular evolution of disk galaxies expected in a Λ CDM universe. Our simulations are organized in a hierarchy of increasing complexity, ranging from rigid-halo collisionless simulations to fully live simulations with gas and star formation. Our goal is to examine which structural properties of disk galaxies may result from secular evolution rather than from hierarchical assembly. In the vertical direction, we find that various mechanisms lead to heating, the strongest of which is the buckling instability of a bar, which leads to peanut-shaped bulges; these can be recognized face-on even in the presence of gas. We find that bars are robust structures that survive buckling and require a large ($\sim 20\%$ of the total mass of the disk) central mass concentration to be destroyed. This can occur in dissipative simulations, where bars induce strong gas inflows, but requires that radiative cooling overcome heating. We show how angular momentum redistribution leads to increasing central densities and disk scale lengths and to profile breaks at large radii. The breaks in these simulations are in excellent agreement with observations, even when the evolution is collisionless. Disk scale lengths increase even when the total disk angular momentum is conserved; thus, mapping halo angular momenta to scale lengths is nontrivial. A decomposition of the resulting profile into a bulge+disk gives structural parameters in reasonable agreement with observations although kinematics betrays their bar nature. These findings have important implications for galaxy formation models, which have so far ignored or introduced in a very simplified way the effects of nonaxisymmetric instabilities on the morphological evolution of disk galaxies.

Subject headings: galaxies: bulges — galaxies: evolution — galaxies: formation —
galaxies: kinematics and dynamics — galaxies: photometry — galaxies: spiral

Online material: color figures, mpeg animation

1. INTRODUCTION

In the current paradigm, galaxy formation is hierarchical (e.g., White & Rees 1978; Steinmetz & Navarro 2002). Indeed, evidence can be found of continued accretion onto both the Milky Way (Ibata et al. 1994; Helmi et al. 1999) and M31 (Ferguson et al. 2002). Although the standard framework of disk formation in such cosmogonies was formulated some time ago (White & Rees 1978; Fall & Efstathiou 1980), disk galaxy formation remains a challenging problem for both simulations (e.g., Navarro & Steinmetz 2000; Abadi et al. 2003) and semianalytical models (e.g., Somerville & Primack 1999; Hatton et al. 2003; van den Bosch 1998, 2000, 2001, 2002; Firmani & Avila-Reese 2000; Mo et al. 1998; Dalcanton et al. 1997; Benson et al. 2003; Cole et al. 1994, 2000; Baugh et al. 1996; Kauffmann et al. 1993). The latest generation of simulations produces disks having roughly the correct sizes and structural properties (Governato et al. 2004;

Abadi et al. 2003; Sommer-Larsen et al. 2003). This is due partly to the increased resolution that reduces the artificial loss of angular momentum of the baryonic component. At the same time, it has been realized that only halos with a quiet merging history after $z \sim 2$ can host disk galaxies today (but see Springel & Hernquist 2005). Therefore, in the current picture most of the mass of the disk is assembled from the smooth accretion of gas cooling inside the dark halo (combined with the accretion along cold filaments for lower mass objects; Katz & Gunn 1991; Katz et al. 2003; Birnboim & Dekel 2003; Kereš et al. 2005) following an intense phase of merger activity that can give rise to the stellar halo and a massive old bulge.

During disk assembly, secular evolution must have played a role in shaping the structure of disk galaxies as we see them at $z = 0$. Nonaxisymmetric instabilities, particularly bars, drive a substantial redistribution of mass and angular momentum in the disk. A possible product of bar-driven evolution is the formation of a bulgelike component. Such a component will have a stellar population similar to that of the disk and is thus younger than the old spheroid formed by the last major merger. Low-mass bulges may result from such a mechanism; observed low-mass bulges

¹ Current address: Astronomy Department, University of Washington, Box 351580, Seattle, WA 98195; debattis@astro.washington.edu.

² Brooks Prize Fellow.

have disklike, almost exponential stellar density (Andredakis & Sanders 1994; Courteau et al. 1996; de Jong 1996; Carollo et al. 1997, 1998, 2001, 2002; Carollo 1999; MacArthur et al. 2003) and in some cases disklike, cold kinematics (Kormendy 1993; Kormendy et al. 2002). Comparison between bulge and disk parameters shows a correlation between the scale lengths of bulges and disks (de Jong 1996; MacArthur et al. 2003) and, on average, similar colors in bulges and inner disks (Terndrup et al. 1994; Peletier & Balcells 1996; Courteau et al. 1996; Carollo et al. 2001). The disklike properties of bulges and the links between bulge and disk properties have been suggested to indicate that bulges may form through the evolution of disk dynamical instabilities such as bars, which are present in about 70% of disk galaxies (Knapen 1999; Eskridge et al. 2000). Further evidence for secular evolution comes from edge-on galaxies, where bulges are often found to be box- or peanut-shaped (Lütticke et al. 2000), a shape associated with evolution driven by the presence of a bar (Combes & Sanders 1981; Pfenniger 1984; Combes et al. 1990; Pfenniger & Friedli 1991; Raha et al. 1991; Kuijken & Merrifield 1995; Bureau & Freeman 1999; Bureau & Athanassoula 1999; Athanassoula & Bureau 1999).

Secular evolution must also be considered for comparisons of predictions based on semianalytic models of disk formation and observations to be meaningful. In the standard picture baryons cooling in dark halos to form a disk have the same specific angular momentum of the dark matter, and this is conserved during collapse. Then the distribution of disk scale lengths can be computed from the known distribution of halo angular momenta (e.g., Dalcanton et al. 1997; Mo et al. 1998; van den Bosch 1998). However, de Jong & Lacey (2000) found that the width of the observed disk scale length distribution at fixed luminosity is smaller than that predicted by such simple models. This suggests that the mapping between initial halo angular momenta and disk scale lengths cannot be so trivial. In addition to complications from the cosmological side, including that the initial specific angular momentum distribution of the baryons need not be like that of the dark halo (e.g., van den Bosch et al. 2002) and angular momentum distributions favoring disks more centrally concentrated than exponential (Firmani & Avila-Reese 2000; van den Bosch 2001; Bullock et al. 2001), secular evolution will also change disk structure. In the simplest prescriptions this is not considered, while it is known since Hohl (1971) that bars can drive substantial evolution of disk profiles.

Which structural properties of present-day disk galaxies are primordial and which are the result of internal evolution? Already by $z \sim 1$ a population of disk galaxies with scale lengths similar to those of a local population is observed (Lilly et al. 1998), suggesting that the structural properties of disk galaxies have not changed substantially since then. If the quiescent phase of disk assembly starts early, as current cosmological simulations suggest, secular evolution might have already been operating by $z = 1$. Verification that the secular evolutionary timescale can be sufficiently short is thus required. With the present algorithms and computing power, simulations of individual isolated galaxies are best able to achieve sufficient force and mass resolution to address such issues. Simulations of individual galaxies decoupled from the hierarchical growth have the additional advantage of exploring directly the role that internal secular evolution plays in shaping the currently observed galaxy population.

In this paper we report on a series of such simulations exploring how disks evolve in the presence of a bar. An important goal of this paper is to demonstrate the wealth of structural properties possible in cosmologically motivated disk galaxies and to

identify what properties of the mass distribution of disk galaxies may result from internal evolution, rather than arising directly from hierarchical assembly. We identify several structural properties we would like to test secular evolution for: vertical thickening, inner profile steepening, profile breaks, and bar destruction. We explore simulations in which the full disk-halo interaction is self-consistent in cosmologically motivated dark matter halos with and without gas and star formation. We use various prescriptions for gas physics, to understand how this impacts the evolution. We also use rigid-halo simulations as in Debattista et al. (2004, hereafter Paper I), which allow us to study a variety of phenomena at high spatial and mass resolution. These simulations also help us to isolate physical mechanisms by which secular evolution occurs. Together these simulations allow us to assess the impact of secular evolution on disk galaxies.

2. METHODS

2.1. Live-Halo Models

Live-halo models are built using the technique developed by Hernquist (1993; see also Springel & White 1999). The structural properties of halos and disks are tied together by the scaling relations expected in the currently favored structure formation model, Λ CDM. We start by choosing the value of the circular velocity of the halo at the virial radius, V_{vir} , which, for an assumed cosmology (hereafter $\Omega_0 = 0.3$, $\Lambda = 0.7$, $H_0 = 65 \text{ km s}^{-1} \text{ Mpc}^{-1}$), automatically determines the virial mass, M_{vir} , and virial radius, R_{vir} , of the halo (Mo et al. 1998). Halos are isotropic and have angular momentum that is specified by the spin parameter, $\lambda = [J^2|E|/(G^2M_{\text{vir}}^5)]^{1/2}$, where J and E are, respectively, the total angular momentum and total energy of the halo and G is the gravitational constant. We use $\lambda = 0.045$ throughout, close to the mean value measured in cosmological simulations (e.g., Gardner 2001). The halo density profile is an NFW (Navarro et al. 1996) with a given value of the concentration c , where $c = R_{\text{vir}}/r_s$, r_s being the halo scale radius. The higher the concentration, the higher the halo density near the center at a given value of M_{vir} (and therefore the more steeply rising is its inner rotation curve). Adiabatic contraction of the halo due to the presence of the disk is taken into account by assuming that the spherical symmetry of the halo is retained and that the angular momentum of individual dark matter orbits is conserved (see Springel & White 1999). The disk mass fraction relative to the halo virial mass, $f_d = M_d/M_{\text{vir}}$, is 0.05, consistent with estimates for galaxies in the local universe (e.g., Jimenez et al. 2003), and is conservatively lower than the estimate of the universal baryonic mass fraction yielded by *WMAP* (Spergel et al. 2003). Our models implicitly assume that the disk forms out of collapsed gas that started with the same specific angular momentum as the halo and that such angular momentum was conserved during infall (Mo et al. 1998). The disk has an exponential surface density profile with scale length R_d that is determined by the value of λ (which sets the degree of available centrifugal support) and by the values of c , f_d , and M_{vir} (which together set the depth of the potential well). The setup of the stellar disk is complete once the Toomre parameter, $Q(R)$, is assigned (Toomre 1964). This corresponds to fixing the local radial velocity dispersion σ_R , since $Q(R) = \sigma_R \kappa / 3.36 G \Sigma_s$, where κ is the local epicyclic frequency, G is the gravitational constant, and Σ_s is the disk surface density. The velocity field of the disk is calculated as in Springel & White (1999; see also Hernquist 1993); in particular, the radial and vertical velocity dispersions are assumed to be equal, and the azimuthal velocity dispersion is determined from the radial dispersion using the epicyclic approximation.

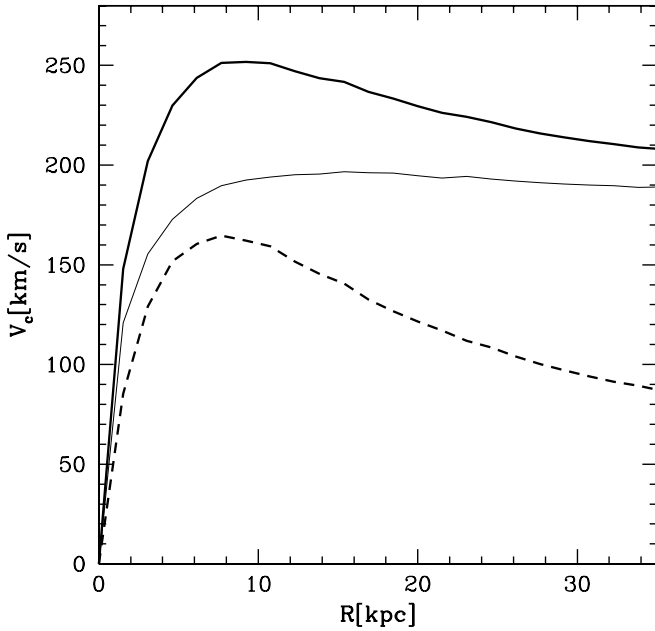


FIG. 1.— Initial rotation curve of the collisionless live-halo models. The thick solid line is the total curve, while the thin solid and dashed lines represent the separate contributions of, respectively, the dark matter and stellar component.

Dark matter halos are sampled using 10^6 particles and stellar disks by 2×10^5 particles. The gravitational softening of both components is equal to 300 pc. We reran a few simulations with higher resolution (5×10^6 halo particles and 5×10^5 disk particles) and smaller softenings (50 pc; see Paper I) to check for resolution effects. We found the analysis presented in this paper to be fairly insensitive to the resolution adopted, and in the remainder we always show results for runs with the standard resolution. The live-halo models used in this paper have structural parameters in line with the expectations of Λ CDM models for a Milky Way-sized system. These models are similar to the mass models of the Milky Way presented by Klypin et al. (2002). The rotation curve of the collisionless models used in the paper is shown in Figure 1. All collisionless models have the same rotation curve since they differ only in terms of their Toomre parameter. These simulations were carried out with the parallel multistep tree code PKDGRAV (Stadel 2001).

2.2. Smoothed Particle Hydrodynamics Simulations

Gasdynamical simulations were carried out with GASOLINE, an extension of PKDGRAV (Stadel 2001) that uses smoothed particle hydrodynamics (SPH) to solve the hydrodynamical equations (Wadsley et al. 2004). The gas is ideal with equation of state $P = (\gamma - 1)\rho u$, where P is the pressure, ρ is the density, u is the specific thermal energy, and $\gamma = 5/3$ is the ratio of the specific heats (adiabatic index). We are assuming that the gaseous disk represents the partially ionized hydrogen component of the galaxy. In its general form the code solves an internal energy equation that includes an artificial viscosity term to model irreversible heating from shocks. The code adopts the standard Monaghan artificial viscosity and the Balsara criterion to reduce unwanted shear viscosity (Balsara 1995). In the adiabatic runs the thermal energy can rise as a result of compressional and shock heating and can drop because of expansion. In runs including radiative cooling energy can be released also through radiation. We use a standard cooling function for a primordial gas composition (helium and atomic hydrogen).

TABLE 1
SAMPLE OF LIVE-HALO SIMULATIONS IN THIS PAPER

Run	M_{disk} ($10^{10} M_{\odot}$)	R_d (kpc)	Q_{star}	f_d	f_{gas}	Q_{gas}	Gas Physics
NC1.....	4.92	3.55	0.7	0.05	0.0
NC2.....	4.92	3.55	1.0	0.05	0.0
NC3.....	4.92	3.55	1.7	0.05	0.0
NG1.....	5.45	3.44	1.7	0.05	0.1	4	RC
NG2.....	5.45	3.44	1.7	0.05	0.1	4	A
NG3.....	5.45	3.44	1.7	0.05	0.1	4	RC+SF
NG4.....	10.9	2.35	1.7	0.11	0.5	0.4	A
NG5.....	5.45	3.44	1.7	0.05	0.5	0.8	RC

NOTES.— M_{disk} , R_d , Q_{star} , and Q_{gas} are the disk mass, initial disk scale length, and the minimum Toomre Q parameter of the stellar and the gaseous disk, respectively. Parameter f_d is the fraction of disk (stars+gas) to dark matter mass, f_{gas} is the fraction of the baryonic mass that is in the gaseous state in the initial conditions, and “Gas Physics” lists the physics of the gas used: “RC” refers to radiative cooling, “A” refers to adiabatic, and “SF” refers to star formation.

Dissipational galaxy models are built following the same prescription described in § 2.1 for live-halo models but include also a gaseous disk represented by 10^5 SPH particles each with a gravitational softening of 300 pc. The basic properties of the runs performed are shown in Table 1. The disk mass fraction is $f_d = 0.05$ in all runs except run NG4, which has $f_d = 0.12$. The gaseous disk has a temperature of 10^4 K, consistent with the gas velocity dispersions derived in observations (Martin & Kennicutt 2001). The gaseous disk has an exponential surface density profile with the same scale length as the stellar disk (see Mayer & Wadsley 2004), and its thickness is determined by local hydrostatic equilibrium. In a gaseous disk the Toomre parameter is defined as $Q(R) = c_s \kappa / \pi G \Sigma_g$, where c_s is the sound speed and Σ_g is the surface density of the gas. The global stability of the disk will be determined by the combined stability properties of the stellar and gaseous disks (Jog & Solomon 1991). Gravitational instabilities can be more vigorous in a cold gaseous disk and might affect the development of nonaxisymmetry even in the stellar disk (Rafikov 2001). In particular, in models having 50% gas, the gaseous disks have $Q < 2$ over most of the radial extent of the galaxy, which should make the system unstable to nonaxisymmetric perturbations irrespective of the stellar Q (see Rafikov [2001] for the case in which the sound speed c_s is ~ 0.3 of the radial stellar velocity dispersion as in our models). In the models with 10% gas instead, the gaseous disk has a high Q , making them stable to axisymmetric perturbations although they still can be unstable to nonaxisymmetric perturbations since $Q < 2$ for the stars (Binney & Tremaine 1987). The Q profiles of gas and stars are shown in Figure 2.

Finally, we also include star formation. The star formation algorithm follows that of Katz (1992), where stars form from cold, Jeans-unstable gas particles in regions of convergent flows (see also Governato et al. 2004; Stinson et al. 2006). The star formation efficiency parameter $c_* = 0.15$, but with the adopted scheme its value has only a minor effect on the star formation rate (Katz 1992). No supernova feedback is included in our simulations. The rotation curve of the models with gas can be seen in Figure 3.

2.3. Rigid-Halo Models

These simulations consist of a live disk inside a rigid halo, which permit large numbers of particles and thus allow high spatial resolution to be reached. High resolution is particularly useful for studying the vertical evolution of disks. Rigid-halo

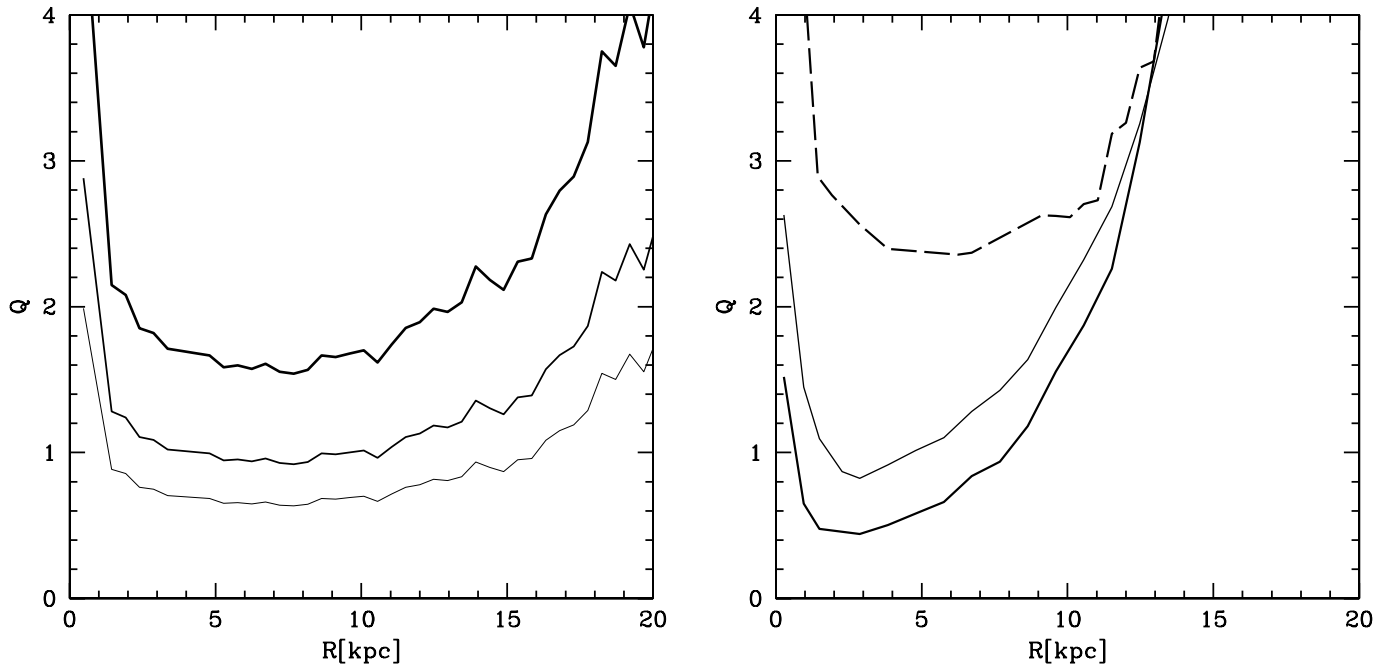


FIG. 2.—Initial Toomre Q profiles for the collisionless live-halo models (*left*) and of those including a gaseous component (*right*). In the left panel we show the profiles of the models used in runs NC1, NC2, and NC3 in order of increasing line thickness. In the right panel we show the Q profile of the gaseous component in run NG4 (*thick solid line*) and run NG5 (*thin solid line*). The Q profile of the gaseous component in runs NG1–NG3 (not shown) is the same as for NG5 except for the normalization being a factor of 5 higher (see Table 1). The Q profile of the stars for run NG4 is also shown (*thick dashed line*). Stellar Q profiles of runs NG1–NG3 and NG5 are equal to that of NC3 except for the normalization (see Table 1).

simulations are better suited to systems in which the disk is dominant in the inner regions because the interaction with the halo is intrinsically weaker (Debattista & Sellwood 2000).

The rigid halos were represented by either a logarithmic potential with a core

$$\Phi_L(r) = \frac{v_h^2}{2} \ln(r^2 + r_h^2) \quad (1)$$

or a cuspy Hernquist model

$$\Phi_H(r) = -\frac{M_h}{r + r_h}. \quad (2)$$

The initially axisymmetric disks were all Sérsic (1968) type,

$$\rho_d(R, z) = \frac{M_d}{2\pi R_d^2} e^{-(R/R_d)^{1/n}} \frac{1}{\sqrt{2\pi} z_d} e^{-(1/2)(z/z_d)^2}, \quad (3)$$

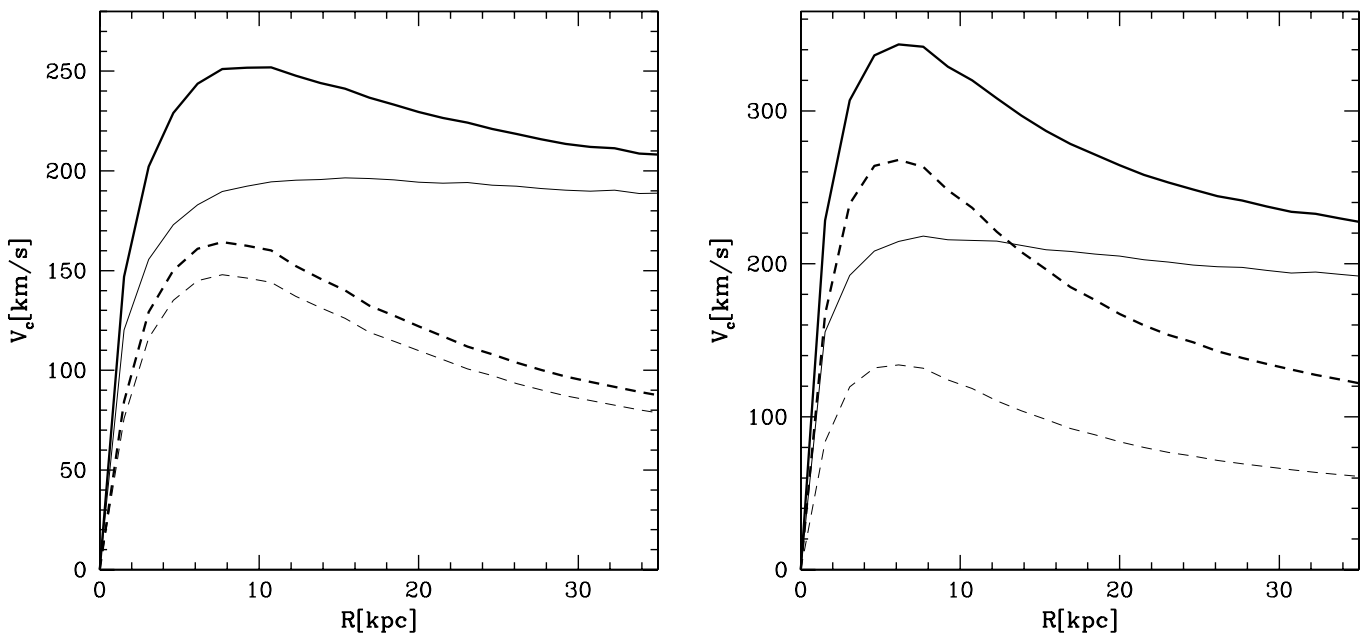


FIG. 3.—Initial rotation curves of the dissipational live-halo models. On the left is the mass model used in runs NG1, NG2, and NG3, and on the right that used in run NG4. The thick solid and thick dashed lines are, respectively, the total curve and the contribution of the baryons (stars+gas), while the thin solid and thin dashed lines represent the separate contributions of, respectively, the dark matter and stellar component. The rotation curve of run NG5 (not shown) is the same as that in the left panel except that the curve for gas gets shifted up by a factor of ~ 1.7 (corresponding to a factor of 5 in mass).

TABLE 2
PRIMARY SAMPLE OF RIGID-HALO SIMULATIONS IN THIS PAPER

Run	z_d/R_d	Q	n	Halo	r_h/R_d	$\ln A_\phi$	$\ln(A_z/R_d)$	B/D	n_b	$R_{b,\text{eff}}/R_{d,f}$	$R_{d,f}/R_d$
L1	0.025	1.6	1.0	Logarithmic	3.3	-1.54	-3.80	0.44	1.1	0.32	1.7
L2	0.05	1.2	1.0	Logarithmic	3.3	-1.15	-3.45	0.52	1.3	0.17	2.1
L3	0.05	1.6	1.0	Logarithmic	3.3	-1.36	-3.77	0.56	0.9	0.47	1.7
L4	0.10	1.2	1.0	Logarithmic	3.3	-1.77	-8.07	0.36	0.8	0.34	1.7
L5	0.10	1.6	1.0	Logarithmic	3.3	-1.36	-7.19	0.69	0.8	0.68	1.5
L6	0.20	1.2	1.0	Logarithmic	3.3	-1.11	-8.07	0.53	0.8	0.44	1.8
S1	0.05	1.0	1.5	Logarithmic	3.3	-0.81	-3.54	0.61	1.8	0.16	2.3
S2	0.05	1.0	2.0	Logarithmic	3.3	-1.20	-3.76	0.76	3.1	0.14	1.5
S3	0.05	1.0	2.5	Logarithmic	3.3	-1.27	-5.91	0.63	1.7	0.12	1.5
H1	0.05	1.2	1.0	Hernquist	20.8	-1.39	-5.68	0.46	1.1	0.22	2.4
H2	0.05	1.6	1.0	Hernquist	20.8	-1.54	-6.83	0.37	1.1	0.51	1.4
H3	0.05	2.0	1.0	Hernquist	20.8	-1.94	-5.22	0.06	1.2	0.70	1.0

NOTES.—Parameters z_d , Q , and r_h are the disk Gaussian scale height, Toomre Q , and halo scale length, respectively. Parameter n is the index of the initial Sérsic disk ($n = 1$ is an exponential disk). In the fifth column we describe the halo type: a logarithmic or Hernquist potential. Parameters $\ln A_\phi$ and $\ln A_z$ are the maximum amplitudes of the bar and of buckling, respectively. Strong buckling corresponds to $\ln A_z \gtrsim -4$. The quantities B/D , n_b , $R_{b,\text{eff}}/R_{d,f}$, and $R_{d,f}$ are all parameters of the bulge+disk decomposition at the end of the simulation. Here $R_{d,f}$ is the final value of the scale length. The following simulations were presented also in Paper II: L2 (as R1), S3 (as R4), L6 (as R6), and H2 (as R7).

with scale length R_d , mass M_d , and Gaussian thickness z_d , truncated at a radius R_t and a Sérsic index n . Disk kinematic setup used the epicyclic approximation to give constant Toomre Q and the vertical Jeans equation to set vertical motions appropriate for a constant thickness. The disks were represented by $(4-7.5) \times 10^6$ equal-mass particles. In units where $R_d = M_d = G = 1$, which gives a unit of time $(R_d^3/GM_d)^{1/2}$, the values for the disk+halo parameters such that our rotation curves were always approximately flat to large radii are given in Table 2. One possible scaling to real units has $R_d = 2.5$ kpc and $V_c = 200$ km s $^{-1}$, so that $M_d = 2.3 \times 10^{10} M_\odot$ and the unit of time is 12.4 Myr. We adopt this time scaling throughout but present masses, lengths, and velocities in natural units.

These simulations were run on a three-dimensional cylindrical polar grid code (described in Sellwood & Valluri 1997) with $N_R \times N_\phi \times N_z = 60 \times 64 \times 243$. We also ran tests with finer grids to verify that our results are not sensitive to the grid used. The radial spacing of grid cells increases logarithmically from the center, with the grid reaching to $\sim 2R_t$ in most cases; except where noted, $R_t = 5R_d$. For all of the simulations in Table 2, the vertical spacing of the grid planes, δz , was set to $0.0125R_d$ (except in run L1, where we reduced this to $0.0083R_d$), but we confirmed that our results do no change with smaller δz . We used Fourier terms up to $m = 8$ in the potential,³ which was softened with the standard Plummer kernel, of softening length $\epsilon = 0.017R_d$, although we also tested smaller ϵ and larger maximum m . Time integration was performed with a leapfrog integrator with a fixed time step, $\delta t = 0.01$ ($\equiv 1.24 \times 10^5$ yr) for all runs with $n = 1$; otherwise, we use $\delta t = 0.0025$ ($\equiv 3.1 \times 10^4$ yr). With these values, a circular orbit at $R_d/10$ typically is resolved into 600 steps. For the logarithmic halos, we set $(r_h, v_h) = (3.3, 0.68)$, while the Hernquist halos had $(r_h, M_h) = (20.8, 43.4)$.

2.4. Tracking Structural Evolution

Our models host disks that are massive enough to form bars in a few dynamical times. The formation of the bar is just one of the mechanisms that drive the morphological evolution of the disks in our simulations. Spiral structure and vertical insta-

stabilities, like the buckling instability, also lead to secular evolution of disk structural parameters, from stellar density profiles and disk scale lengths to the bulge-to-disk ratio. In order to track the evolution of our models, we measured the amplitude of the bar, A_ϕ , as the normalized amplitude of the $m = 2$ density distribution:

$$A_\phi = \frac{1}{N} \left| \sum_j e^{2i\phi_j} \right|, \quad (4)$$

where ϕ_j is the two-dimensional cylindrical polar angle coordinate of particle j . The sum extends over stellar particles only. We measured the $m = 2$ bending amplitude, A_z , similarly:

$$A_z = \frac{1}{N} \left| \sum_j z_j e^{2i\phi_j} \right|. \quad (5)$$

These quantities allowed us to determine when a bar formed and whether it buckled.

3. VERTICAL EVOLUTION

The vertical direction is best resolved in the rigid-halo simulations, so we begin by considering those. By far the fastest secular evolution in the vertical direction is driven by the buckling instability. This bending instability, which is caused by anisotropy, is very efficient at heating the disk vertically.

Raha (1992) described the distortion of a bar during buckling. As that work is not widely available, we present a description of buckling in run L2 before exploring its effects on stellar disks. In the animation accompanying this paper (see also Fig. 4) we show the evolution of this run between $t = 1.0$ and 2.2 Gyr. At $t = 1.12$ Gyr, the system is largely symmetric about the mid-plane but develops a small bend by $t = 1.18$ Gyr, which displaces the center toward positive z and the outer parts of the bar toward negative z . In the outer parts of the bar, where it has its largest vertical excursion, the bend develops on the leading side of the bar where it persists for some time, eventually evolving into a trailing spiral. As it passes the major axis of the bar, it grows substantially. After this bend has dissipated, the process repeats another two times (see also Martinez-Valpuesta et al. 2006), with small bends on the leading side of the bar, developing into stronger bends on crossing the bar's major axis. At smaller radii within the bar, the peak bending amplitude occurs close to

³ In order that models remain centered at the origin, we excluded the $m = 1$ term in the expansion. Including this term would result in large but artificial offsets between the bar and the center, similar to the ones found by McMillan & Dehnen (2005).

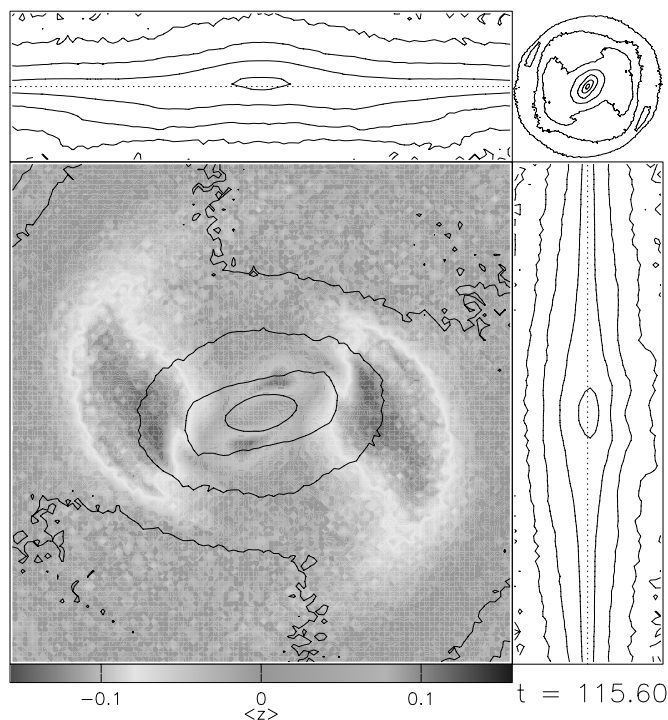


FIG. 4.—Bending in run L2 at the peak of the bend, $t = 1.43$ Gyr in our adopted scaling. [See the electronic edition of the *Journal* for a color version of this figure, which is also available as an *mpeg* file in the electronic edition.]

the minor axis (e.g., at $t = 1.43$ Gyr). The region outside the bar also bends (e.g., at $t = 1.55$ Gyr), but generally with smaller amplitude. Small-scale bending persists to late times and is still ongoing as late as $t = 2.60$ Gyr. At $t \simeq 1.42$ Gyr, the buckling produces the largest mean vertical displacement, $\bar{z} \simeq 0.157R_d$, which is more than 3 times the initial disk thickness for this simulation, $z_d = 0.05R_d$.

Buckling leads to a significant vertical heating: at the center σ_w/σ_u increases from ~ 0.4 to ~ 0.85 , and σ_w/σ_u averaged inside $R = 1.2$ increases by a similar factor, where σ_w is the vertical velocity dispersion and σ_u is the radial velocity dispersion. The three phases of strong bending (which can be seen in the accompanying animation) can be identified with three phases of strong vertical heating.

3.1. Peanuts from Buckling

After buckling, model L2 becomes distinctly peanut shaped when viewed edge-on. The disk scale height h_z has increased by factors of 2–6 depending on where it is measured. It is larger on the minor axis of the bar than on the major and is smallest at the center, properties that are typical of all of the rigid-halo simulations but are more pronounced for the buckled bars (see also Sotnikova & Rodionov 2003). The peanut results in a negative double minimum in d_4 , the fourth-order Gauss-Hermite moment (Gerhard 1993; van der Marel & Franx 1993) of the density distribution (i.e., the peanut produces a flat-topped density distribution) *within the bar*. The peanut is also manifest in the face-on kinematics as a pronounced negative minimum in the Gauss-Hermite kinematic moment, s_4 .⁴ No similar signature of a peanut is evident before buckling. In Debattista et al. (2005, hereafter

⁴ We use Gauss-Hermite moments in which the velocity scale is the rms velocity. In order to distinguish this from the more commonly used best-fit Gaussian scale, we refer to this moment as s_4 rather than h_4 .

Paper II) we developed this into a diagnostic signature of peanuts seen nearly face-on.

Buckling need not always result in a peanut. Both models L1 and L2 formed strong bars and had roughly equal buckling that vertically heated both disks substantially. However, whereas L2 formed a strong peanut, L1 formed only a weak one.

3.2. Vertical Heating with Live Halos and Gas

The vertical heating of disks in our simulations with live halos is dominated by the buckling instability when gas is absent. When gas is present, we found that it may suppress buckling, in agreement with Berentzen et al. (1998). (We tested that this result does not depend on force resolution by repeating runs with a softening 6 times smaller, i.e., 50 pc.) But this depends on how readily gas dissipates its thermal energy (see Fig. 10), a point not appreciated by Berentzen et al. (1998), who performed only isothermal simulations. When the gas can cool (NG1), buckling is suppressed. In this case the bar amplitude decreases significantly because of the central gas concentration produced in the inflow driven by the bar. The reduced bar strength implies a reduced radial anisotropy in the system, which then is less prone to buckling (Berentzen et al. 1998). However, the bars in the 10% gas case are not destroyed (see § 4), which suggests that the complete suppression of buckling does not simply reflect the decrease in bar strength. This is evident especially in run NG3, which has gas cooling and star formation, in which a fairly strong bar is present and yet buckling did not occur. In Berentzen et al. (1998) weak buckling was always associated with weak bars.

In axisymmetric systems, central concentrations suppress bending modes (Sotnikova & Rodionov 2005). Demonstrating a similar result in the barred case in the presence of gas is nontrivial. Indeed, whether gas suppresses buckling directly because it can dissipate bending energy or because it leads to central mass concentrations (Berentzen et al. 1998) proved difficult to determine because any experiment we could conceive of also led to different bars. For example, when we replaced the central (inner 600 pc) gas blob formed in run NG1 after ~ 2 Gyr with a point mass having equal mass and softening equal to its half-mass radius and evolved the system as purely collisionless, we found that the bar buckled, but in the meantime it also grew stronger. While we were not able to design a clear test for these two hypotheses, our results do exhibit a correlation between buckling amplitude and central mass concentration (Fig. 5).

Vertical heating in the presence of gas occurs even without buckling, as shown in Figure 6. In NG1 and NG3, in which no buckling occurs, we still see an increase in the vertical stellar velocity dispersion. This heating is gentle, with σ_z/σ_R increasing nearly linearly with time and never falling below the critical threshold of ~ 0.4 . The cause of this vertical heating appears to be scattering by spirals in the gas disk, which remains significantly thinner than the stellar disk in this simulation. In contrast, heating by buckling, as in run NG2 (in which the gas disk quickly became thicker than the stellar disk), is abrupt. The gas thickness in this simulation results from a steadily increasing temperature as a result of shock heating.

3.3. Peanuts without Buckling

The live-halo simulations show an alternative way in which peanuts can form. The gas-free live-halo simulations all buckled and in the process formed peanuts no different from those described above. In some simulations with gas (e.g., NG3) we found peanuts forming without buckling. It is possible that these formed by direct resonant trapping of orbits in the growing bar

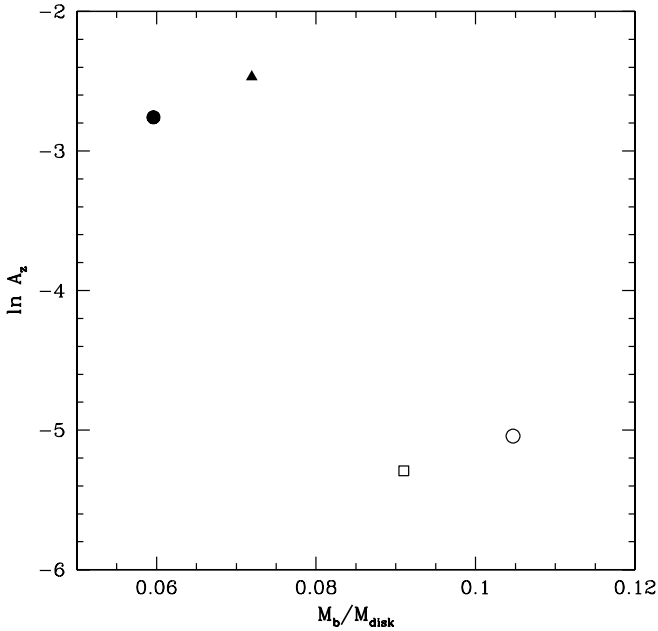


FIG. 5.— Correlation between central mass concentration and the maximum strength of the buckling instability in the live-halo simulations. NC3 is indicated by a filled circle, NG2 by a filled triangle, NG1 by an open circle, and NG3 by an open square. The central mass concentration is measured using the baryonic (stellar+gaseous) mass within 800 pc relative to the total disk mass (the disk is always the dominant mass component inside 1 kpc in these models).

potential (Quillen 2002). Indeed, in run NG3 A_ϕ increased by a factor of about 2 over a period of ~ 2 Gyr (Fig. 10).

3.4. Peanuts in the Presence of Gas

We showed in Paper II that peanuts produce prominent minima in the kinematic Gauss-Hermite moment, s_4 , when viewed face-on. In Figure 7 we show that a peanut can still be recognized by a prominent negative minimum in s_4 in model NG2, despite the presence of gas. The reason for this is that the gas sinks to smaller radii than the peanut.

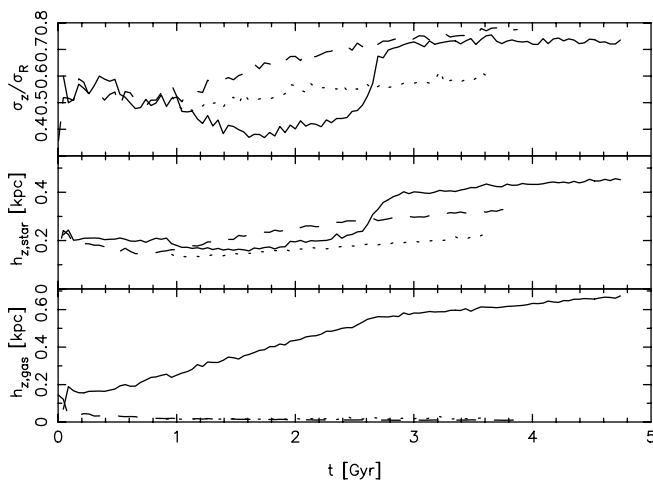


FIG. 6.— Vertical heating in models NG1 (dashed line), NG2 (solid line), and NG3 (dotted line). The top panel plots the ratio of vertical to radial velocity dispersions at the center of the disks as a proxy for vertical heating. The middle and bottom panels show the central scale heights of stellar and gaseous disks, respectively. NG2 buckles, which results in the strong vertical heating seen at ~ 2.5 Gyr, while the bars in NG1 and NG3 never buckle. But because their gas disks remain much thinner than the stellar disks, they continue to heat it vertically over a long time.

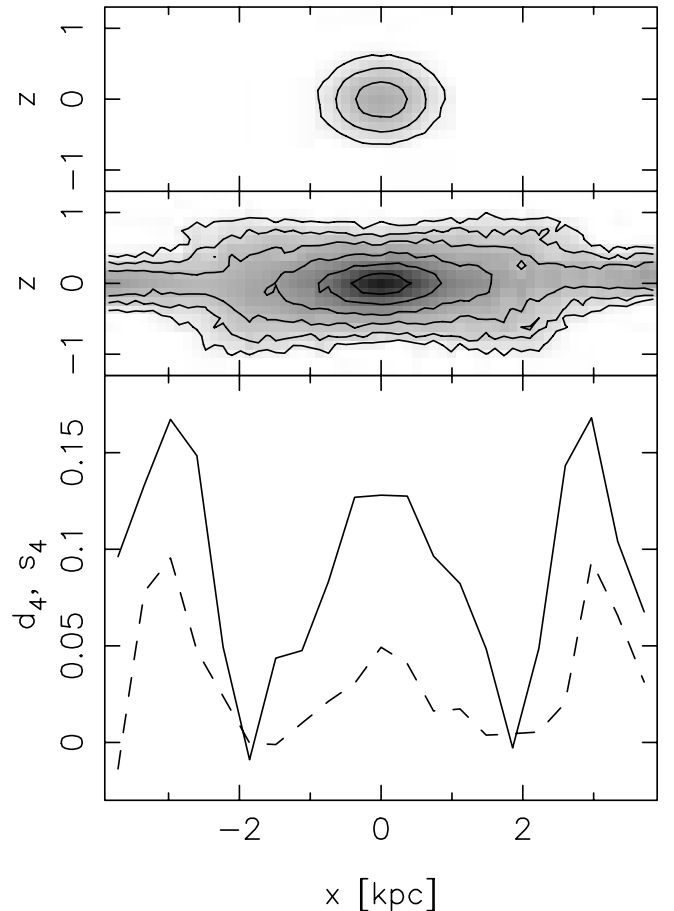


FIG. 7.— Peanut in model NG2. The top panel shows the edge-on gas density in the region $|y| \leq 1$ kpc, while the middle panel shows the stellar edge-on density (in the region $|y| \leq 1$ kpc). The bottom panel plots d_4 (solid line) and s_4 (dashed line).

4. BAR DESTRUCTION

Both the buckling instability and the growth of massive central objects have been suggested to destroy bars. We examine each of these in this section.

4.1. The Collisionless Case

After Raha et al. (1991) showed that buckling weakens bars, it has often been assumed that bars are destroyed by buckling. To our knowledge, that buckling destroys bars has never been demonstrated; indeed, none of the bars in our simulations were destroyed by buckling. Merritt & Sellwood (1994) noted that buckling grew stronger when force resolution was increased because then particles have larger vertical oscillatory frequencies, destabilizing the bar. Thus, the most damaging buckling occurs in the rigid-halo simulations, where the vertical structure is best resolved. We verified that the survival of bars after buckling is not due to insufficient resolution by running an extensive series of numerical tests at higher resolution using rigid halos. For these tests, we used model L2, one of the most strongly buckling simulations. The bar amplitude A_ϕ after buckling in these tests turned out to not be strongly dependent on any numerical parameter. Thus, that buckling does not destroy bars is not an artifact of insufficient resolution. This conclusion is also supported by a higher resolution version of the live-halo simulation of Paper I, where we increased the number of particles ($N_{\text{halo}} = 4 \times 10^6$, $N_{\text{disk}} = 2 \times 10^5$) and decreased the softening ($\epsilon = 50$ pc for all

particles). Again, although buckling was strong here as well, the bar was not destroyed.

We also checked that increasing spatial resolution does not lead to stronger buckling in weakly buckling simulations. We reran simulations L5 and H1 at higher resolution ($m = 32$, $\delta z = 0.005$, and $\epsilon = 0.0083$) and found that A_ϕ is barely affected, demonstrating that vertical frequencies were well resolved and confirming that the weak bucklings are intrinsic.

4.2. The Effect of Bar Slowdown

Although our grid code simulations have high resolutions, they have rigid halos; thus, bar slowdown (Weinberg 1985; Debattista & Sellwood 1998, 2000; Sellwood & Debattista 2006) is not included. Araki (1985) showed that stability to bending modes in the infinite, uniform, nonrotating sheet required that $\sigma_w \geq 0.293\sigma_u$. As a bar slows, σ_u is likely to increase, which may drive a stable bar to instability. To test whether this happens, we slowed down some of our bars by introducing a retarding quadrupole moment

$$\Phi_{\text{ret}} = \Phi_0 f(R) g(s) e^{-2i(\phi_{\text{bar}} - \phi_r)} \quad (6)$$

trailing behind a bar. Here $s = (t - t_0)/(t_1 - t_0)$ and $g(s) = -16s^2(1 - s)^2$, so that the perturbation is gently switched on at t_0 and off at t_1 . The phase of the bar, ϕ_{bar} , was computed at each time step by computing the phase of the $m = 2$ Fourier moment of all of the particles; since the disk also has spirals, there is a typical uncertainty of order $\pm 15^\circ$ in the bar angle. We therefore set $\phi_r = 30^\circ$ to be certain that the retarding potential always trails the bar. We chose the radial dependence of the retarding potential to be $f(R) = R/(1 + R^2)^2$, which ensured that it peaks inside the bar radius.

We performed these experiments on runs L2, L4, and H2; a list of all of the experiments is given in Table 3. For run L2, we switched on the quadrupole shortly after the bar formed and switched it off before it buckled. In this case we found that the buckling is then stronger, which leaves the bar $\sim 20\%$ weaker but still does not destroy it.

The other two systems on which we tried such experiments had not buckled when undisturbed. In these cases, we turned on the retarding quadrupole after the bar had settled and turned it off not less than 1.5 bar rotations later. Slowing down these bars resulted in very strong buckling, stronger even than in run L2. But even in these somewhat extreme cases the bar survives; we illustrate this in Figure 8, where we show the various bar slowdown experiments in model H2. While these bucklings do not destroy

TABLE 3
SERIES OF SIMULATIONS TO TEST THE EFFECT OF BAR SLOWDOWN
ON THE BUCKLING INSTABILITY

Run	Φ_0	t_0 (Gyr)	t_1 (Gyr)
L2.s1.....	16	0.74	1.24
L2.s2.....	1.6	0.74	1.24
L4.s1.....	1.6	2.60	3.10
L4.s2.....	4.8	2.60	3.10
H2.s1.....	4.8	2.60	3.10
H2.s2.....	1.6	2.60	3.10
H2.s3.....	0.8	2.60	3.10
H2.s4.....	0.8	2.60	3.72

NOTE.—Parameter Φ_0 measures the relative amplitude of the retarding perturbation, while t_0 and t_1 give the time when the perturbation is switched on and off, respectively.

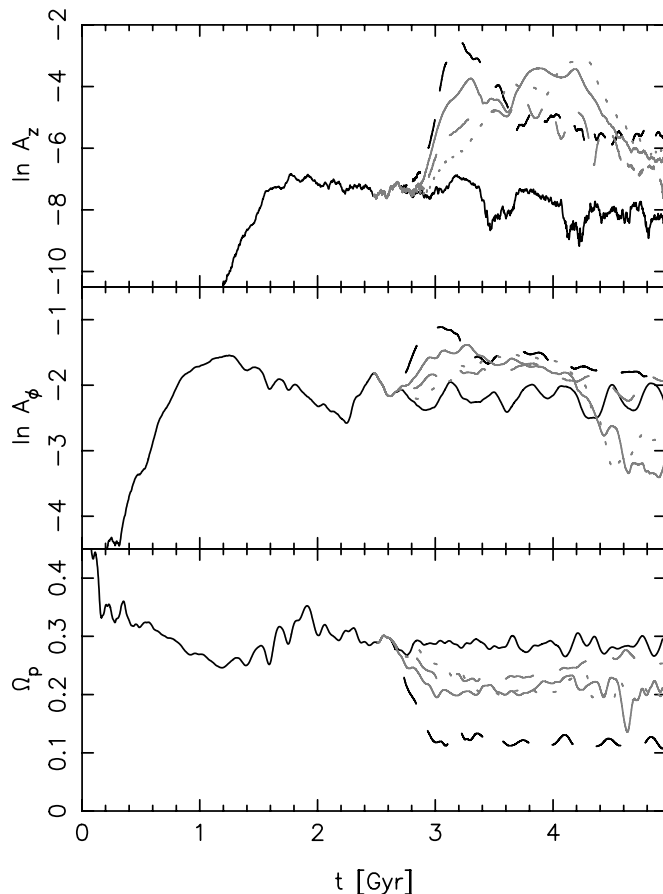


FIG. 8.—Effect of bar slowdown in run H2: whereas the unsloped bar suffers only a weak bend, slowdown leads to a fierce buckling. However, the bar still survives. The top and middle panels show the buckling and bar amplitudes, respectively, while the bottom panel shows the evolution of the bar pattern speed, Ω_p . The black solid and dashed lines and the gray solid, dashed, and dotted lines show runs H2, H2.s1, H2.s2, H2.s3, and H2.s4, respectively.

bars, which we determine simply by visual inspection, in a few cases they leave a much weaker bar, which would be better described as an SAB than an SB. In Figure 9 we present the most extreme example of H2.s4, in which the final bar axis ratio was $b/a \simeq 0.85$; although weak, this can still clearly be recognized by visual inspection. The edge-on view of a slice taken around the bar's major axis reveals a peanut, which can be recognized by the double minimum in s_4 diagnostic. These slowed bars probably represent an upper limit to the damage buckling can inflict on strong bars.

In the live-halo simulations, where the bar can interact with the halo and slow down, we continue to find that buckling does not destroy bars. Therefore, we conclude that the bar buckling instability does not destroy bars (see also Martinez-Valpuesta & Shlosman 2004).

4.3. Central Gas Mass Growth

We now consider bar destruction via the growth of a massive central gaseous object. The bottom panel of Figure 10 shows the evolution of the bar amplitude for models NG1–NG3. The bar amplitude depends very strongly on the gas physics: when the gas is adiabatic (NG2), it does not become very centrally concentrated and the bar amplitude is not very strongly affected by the gas. If the gas can cool (NG1), it sinks quickly to the center and remains there. Thus, the bar forms already much weaker. Continued infall at later times further weakens the bar. The main

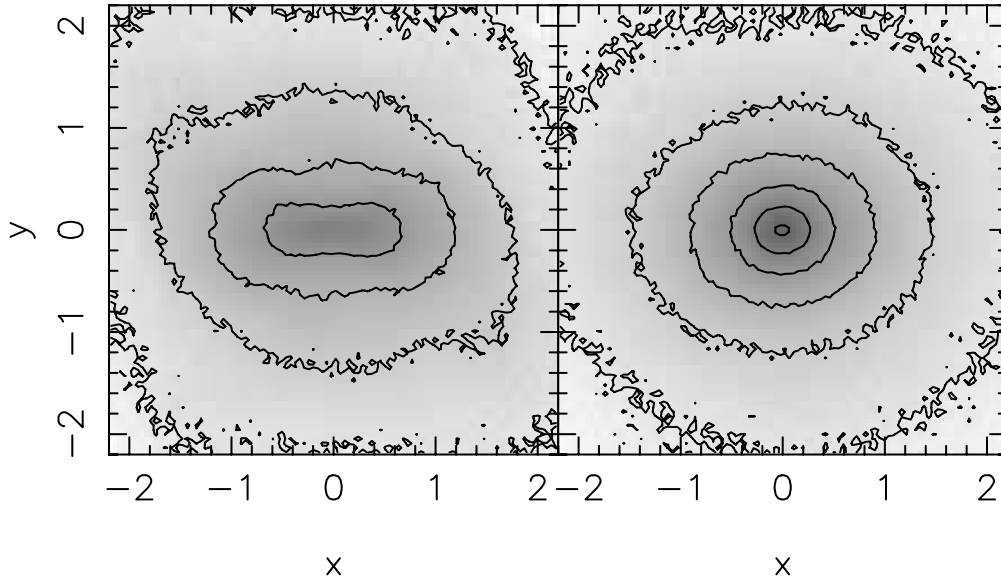


FIG. 9.—On the left is H2.s4 at $t = 4.96$ Gyr, showing that before buckling the bar was prominent. On the right the system is shown at $t = 12.4$ Gyr, well after the imposed bar slowdown. The bar never fully recovers from the strong buckling, and the system is better described as weakly barred.

difference between the cooling and adiabatic simulations is in the amount of gas that sinks into the center of the disk. In NG1, gas accounts for $\sim 60\%$ of the mass within 500 pc (Fig. 11); with such a high fraction, it is unsurprising that the bar is weaker. The softening in these simulations is 300 pc; therefore, the central gas mass is not well resolved. At these scales the hydrodynamical resolution is higher than the gravitational force resolution (the

gravitational softening volume contains many times the SPH smoothing volume) with the result that the collapse of gas toward the center is inhibited (see Bate & Burkert 1997). Therefore, the same amount of gas would probably have collapsed to an even smaller radius had we had greater force resolution, weakening the bar further. In NG2 gas cannot radiate away the intense

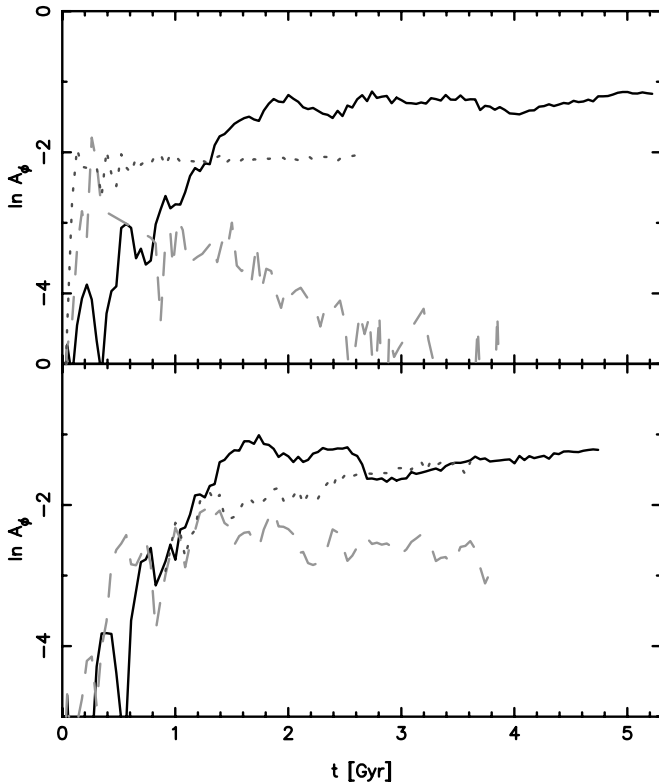


FIG. 10.—Effect of gas on bar amplitudes. The top panel shows the evolution of the bar amplitude in runs NC3 (solid line), NG4 (dotted line), and NG5 (dashed line). The bottom panel shows the evolution for runs NG1 (dashed line), NG2 (solid line), and NG3 (dotted line). [See the electronic edition of the Journal for a color version of this figure.]

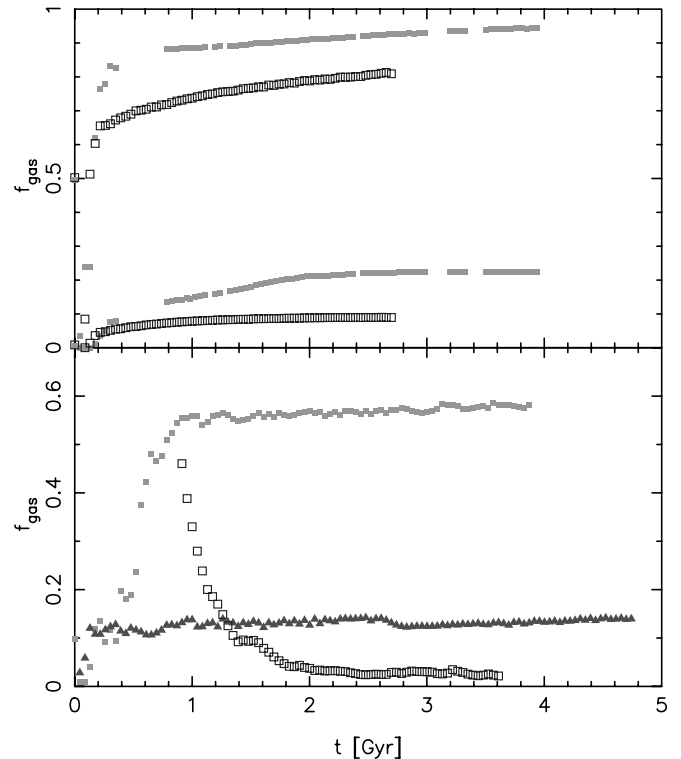


FIG. 11.—Gas mass fraction inside 500 pc in the 10% gas mass runs (bottom) and the 50% gas mass runs (top). The bottom panel shows NG1 (filled squares), NG2 (filled triangles), and NG3 (open squares). The top panel shows NG4 (open squares) and NG5 (filled squares). The lower set of points in this panel show the fraction of the total disk mass that is inside 500 pc; for the cooling simulation, this fraction is large enough to destroy the bar. [See the electronic edition of the Journal for a color version of this figure.]

compressional heating it experiences, and only 10% by mass is found within 500 pc. Thus, its bar is stronger than in NG1. When star formation is allowed (NG3), the gas accumulated into the center drives a starburst. This converts most of the highly concentrated gas into stars, which can now support the bar. A strong bar again forms. Since our simulations do not include feedback, none of the mass that falls in flows back out; up to $t \sim 2.5$ Gyr, there is very little difference in the (azimuthally averaged) density profile inside 3 kpc between runs NG1 and NG3. Later profile differences are most likely caused by the difference in the bars, which, being stronger in run NG3, leads to further infall to the center.

Not much changes at higher gas mass fraction if the gas is adiabatic (NG4). Then the gas layer is quite thick, producing a bar that, although somewhat weaker than in the purely stellar case (NC3), is still quite strong. When the gas can cool (NG5), the gaseous disk becomes violently gravitationally unstable and a new phenomenon appears, namely, the fragmentation of gas into clumps that sink to the center, dragging an associated stellar clump. Such clump instabilities have been found in previous simulations (Noguchi 1999; Immeli et al. 2004) and have been shown to build central bulglike objects directly. Immeli et al. (2004) showed that the rate at which clouds dissipate their energy is the main parameter that determines whether the clump instability occurs. As a result of the central mass, only a weak bar forms, and this is eventually destroyed by continued gas inflow.

In our fully self-consistent simulations with cosmologically motivated halos, we found that the fraction of the total disk mass needed to destroy the bar ($\sim 20\%$; Fig. 11) is in very good agreement with that recently found by Shen & Sellwood (2004), as is the gradual decay of the bar amplitude (Fig. 10). This result is different from that of Bournaud et al. (2005); we note that our model NG5 differs from theirs in two important ways. NG5 has a live halo versus their rigid halos, and the dark matter halo is strongly concentrated at the center. Both properties of our halos allow angular momentum to be transferred from bar to halo efficiently (Weinberg 1985; Debattista & Sellwood 1998), which may perhaps account for the difference in these results.

5. INNER PROFILE EVOLUTION

We explore the evolution of density profiles at large radii in § 6, and in § 7 we discuss the bulge+disk decompositions that result from profile evolution. In this section we explore this evolution qualitatively.

5.1. Buckling and Central Densities

Bar formation leads to a change in density profiles. As was already noted by Hohl (1971), the central density generally increases while the outer disk becomes shallower. In Figure 12 we show that bar formation leads to an increase in the central density in run L2 (here we define central density from particle counts inside $0.1R_d \simeq 5\epsilon$). Moreover, as already noted by Raha et al. (1991), buckling may also increase the central density of a disk. We demonstrated *directly* that buckling is responsible for an increase in central density by resimulating this system with an imposed symmetry about the midplane, which prevents buckling. Figure 12 shows that when buckling is absent, no further increase in central density occurs. The buckled system is 2.0 times denser at the center than when it is prevented from buckling.

5.2. Disk Scale Lengths and Angular Momentum

In Paper I we argued that the fact that the evolution of the scale length of the outer disk changes under the influence of the bar, even when the total baryonic angular momentum is conserved,

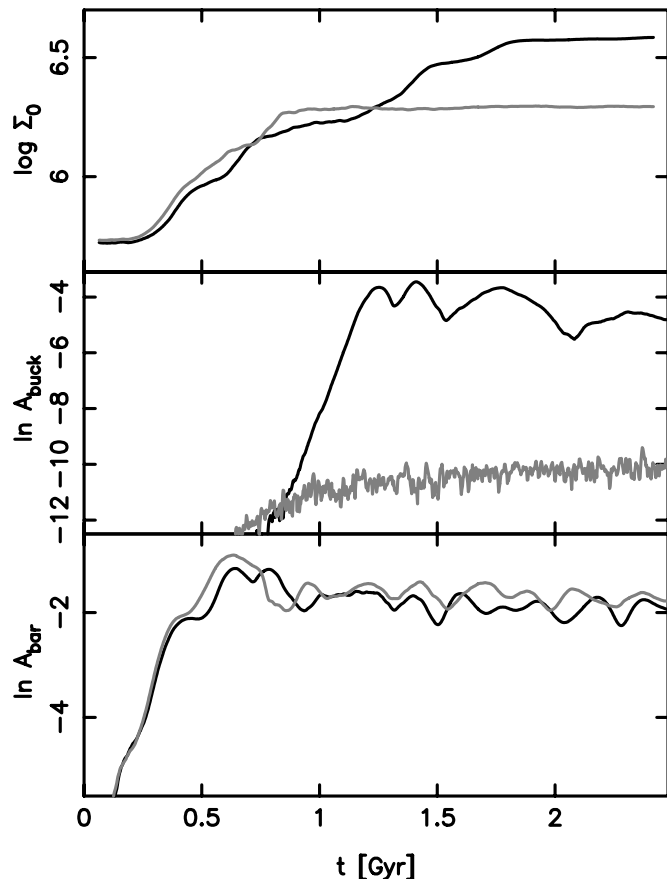


FIG. 12.—Evolution of the central density obtained from particle counts within $0.1R_d$ (top) in the strongly buckling run L2 (black line) and the run with imposed midplane symmetry (gray line). The bottom panel shows the evolution of bar amplitude, which reaches similar values in both runs. The middle panel shows the buckling amplitude. The gray lines show the evolution when symmetry about the midplane is imposed; while there is little difference in bar amplitude, no buckling can occur.

implies that the distribution of disk scale lengths does not follow automatically from that of halo angular momenta. The increase in disk scale length is due to transfer of angular momentum from the bar to the outer disk (Hohl 1971). It is remarkable that the disk outside the bar remains exponential out to the point where a break occurs, in both collisionless and dissipative systems. Hohl (1971) was the first to notice that exponential disks are naturally obtained after bar formation (outside the bar) even when the initial disk did not have an exponential profile. Since bars are ubiquitous in galaxies at low and high redshift (Jogee et al. 2004), it follows that the effect of secular evolution on disk sizes has to be included in any realistic galaxy formation model.

Not only do bars change disk scale lengths, but the amount by which they change varies dramatically depending on the Q profile, even for (nearly) identical initial angular momentum. Consider models H1, H2, and H3. These all have the same initial conditions other than Toomre Q , leading to $\lesssim 10\%$ difference in the total baryon angular momentum. Nevertheless, the final values of R_d range from 1.0 to 2.4 (Table 2). We conclude that the direct mapping of halo spins into a distribution of disk scale lengths (e.g., Mo et al. 1998) will not yield correct predictions.

6. OUTER DISK BREAKS

Disk densities do not always exhibit a single exponential profile. More typically a sharp break between an inner and outer profile is evident. These breaks are often referred to as truncations

TABLE 4
SIMULATIONS TESTING DISK BREAKS

Run	R_t/R_d	Q
L2.t8	8	1.2
L2.t12	12	1.2
L4.t12	12	1.2
L5.t12	12	1.6
H1.t12	12	1.2
H2.t12	12	1.6
H3.t12	12	2.0
T1.t12	12	1.2

NOTES.—The first two characters in the name of each simulation reflect the model from Table 2 on which that simulation is based by extending R_t from $5R_d$ to either $8R_d$ or $12R_d$ (number after “t” in the name of each run). Model T1.t12 is not based on any in Table 2. It was produced by adding to run L2 a central Gaussian: $\Sigma(R) = \Sigma_0(e^{-R/R_d} + 4e^{-1/2(R/0.2)^2})$.

following the apparently sharp drop-offs first discovered by van der Kruit (1979). Subsequently, van der Kruit & Searle (1981a, 1981b) fitted sharp truncations to light profiles at large radii. However, de Grijs et al. (2001) found that truncations occur over a relatively large region, rather than sharply. The larger sample of Pohlen (2002) confirmed this result; he found that truncations are better described by a double exponential profile with a break radius. For his sample of mostly late-type systems, Pohlen (2002) estimates that the fraction of disk galaxies with breaks is $\approx 79\%$. Similar disk breaks have been found up to redshifts of $z \approx 1$ (Pérez 2004; Trujillo & Pohlen 2005). What is the origin of these features in the light distribution of disks? In § 5 we showed that the angular momentum redistribution caused by the bar leads to an increased central density and a shallower density profile outside this. This angular momentum redistribution cannot be efficient to arbitrarily large radii; thus, we may ask whether secular evolution can give rise to breaks in density profiles.

Studying breaks in N -body simulations is numerically challenging because they generally occur at large radii, where the density of particles is low. We therefore ran several high-resolution rigid-halo simulations with disks extended as far as $R_t = 12R_d$; with 7.5 megaparticles the initial conditions still had ~ 24 kiloparticles

at $R \geq 8R_d$ and >3 kiloparticles at $R \geq 10R_d$, sufficient to properly measure the density profile out to the large radii required. We chose R_t this large in order to ensure that edge modes (Toomre 1981) do not interfere with other secular effects. The series of simulations we used in this study is listed in Table 4.

In order to compare our simulations with observations, we used the double exponential fitting form of Pohlen (2002). We only fit profiles at $2R_d \leq R \leq 8R_d$; the lower limit is needed to avoid the central bulgelike component. At very large radii, the surface density barely evolves because of the low self-gravity (although all of our models were evolved for at least three rotations at the outermost radius). Clearly the profile at larger radii reflects only our initial conditions. A reasonable transition radius between the initial profile and the secularly evolved profile occurs at $R \approx 8R_d$, which we use as our upper limit on the double exponential fits. (For the initial pure exponential profile this is equivalent to ~ 7 mag fainter than the center.)

These fits give three dimensionless quantities: R_{br}/R_{in} , the ratio of break radius to inner scale length, R_{out}/R_{in} , the ratio of outer scale length to inner scale length, and $\mu_{0,in} - \mu_{0,out}$, the difference between the central surface brightnesses of the two exponential fits, which we compare with the data of Pohlen et al. (2002) and Pohlen & Trujillo (2006).

6.1. The Face-on View

Several of our simulations produced clear breaks of the double exponential type. We present one example in Figure 13, where we show the initial and final profiles in run L2.t8. The profile very quickly develops from a single exponential to a double exponential. In Figure 14 we plot the evolution of the parameters of the double exponential profile for this run and for runs L2 and L2.t12. The formation of the break in these three simulations is obviously a discrete event. Their bars formed at $t \approx 620$ Myr; R_{br} does not evolve substantially after $t \approx 990$ Myr. Because of this near coincidence in time, we conclude that, in these simulations, the process of bar formation can directly or indirectly somehow lead to the formation of broken profiles.

Figure 14 also investigates the difference between $R_t = 8R_d$ (black lines), $12R_d$ (thick gray lines), and $5R_d$ (thin gray lines) (models L2.t8, L2.t12, and L2, respectively). The similarity of the break parameters in the three simulations shows that the breaks do not result from edge modes (Toomre 1981). In run L2,

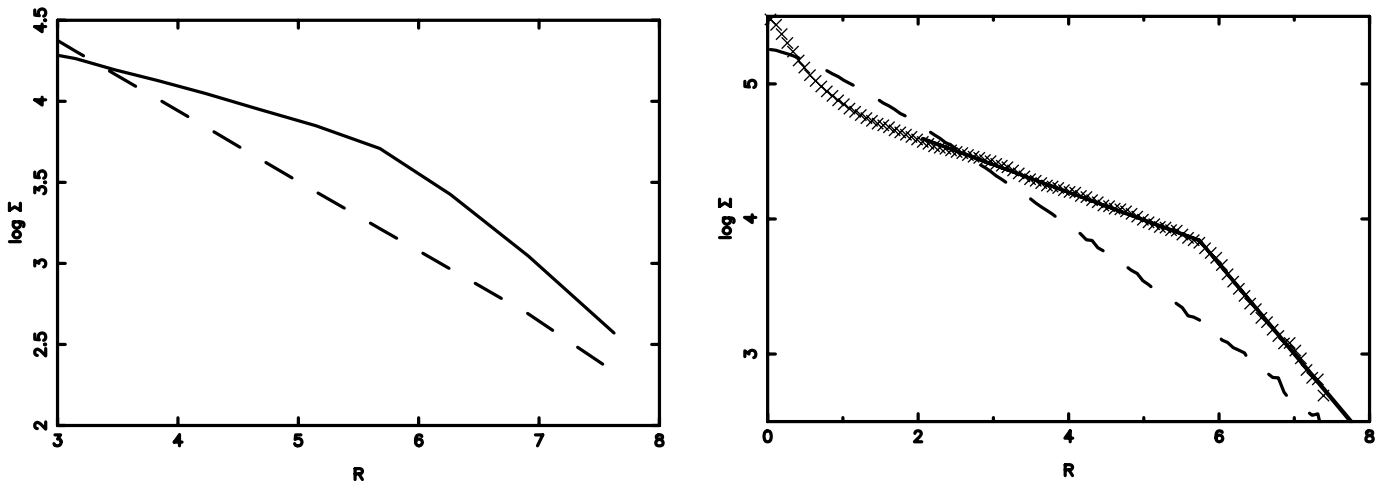


FIG. 13.—Density profile of run L2.t8 at large radii showing the formation of a break. The left panel shows the azimuthally averaged face-on density profile, with the dashed line showing the initial conditions and the solid line showing the final profile. In the right panel, which shows the edge-on profile, the two solid lines indicate the exponential fits over their respective regions, while the crosses show the surface brightness. The dashed line shows the edge-on profile of the initial exponential disk.

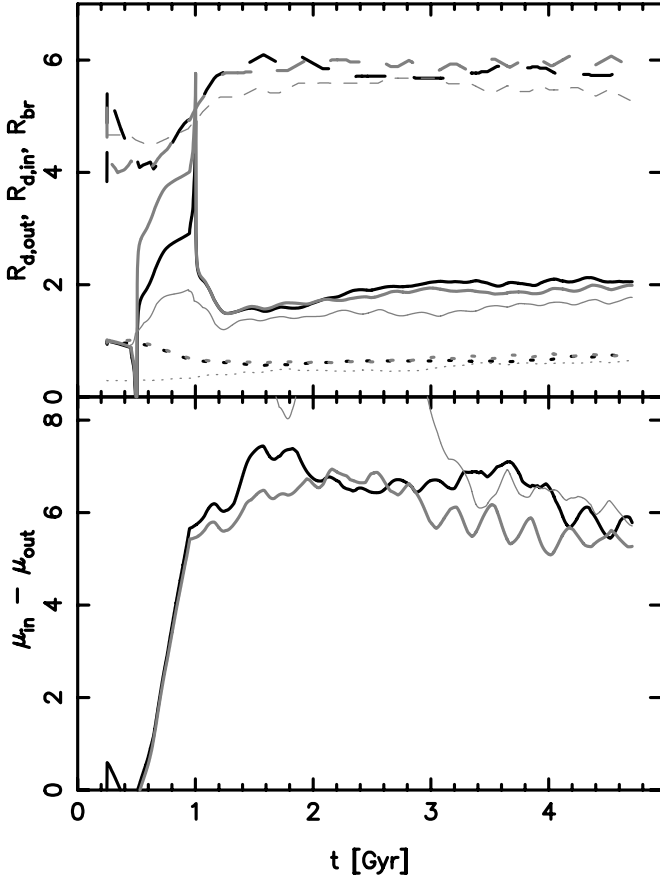


FIG. 14.—Evolution of the break in the face-on surface density. In the top panel we show R_{out} (dotted lines), R_{in} (solid lines), and R_{br} (dashed lines). The black lines show run L2.t8 ($R_t = 8R_d$), the thick gray lines show run L2.T12 ($R_t = 12R_d$), and the thin gray lines show run L2 ($R_t = 5R_d$).

the initial disk did not extend as far as the final break radius; thus, the break is not an artifact of our initial disk extending to very large radii. Therefore, all parameters of the double exponential profile that develops can be considered robust.

In Figure 15 we compare the break parameters of the simulations with the observations of Pohlen et al. (2002) and Pohlen & Trujillo (2006) for a combined sample of 31 face-on galaxies. Our simulations are in reasonable agreement with the observations, although they span a smaller part of the parameter space. The agreement in the narrow distributions in the $(R_{\text{out}}/R_{\text{in}}, \mu_{0,\text{in}} - \mu_{0,\text{out}})$ -plane is quite striking.

We explore the angular momentum redistribution that leads to the breaks in Figure 16. This plots the distribution of angular momenta in the initial conditions and at the end of the simulation for runs H1.t12 (with $R_{\text{br}} \simeq 5R_d$) and H3.t12 (which did not form a break). In the left panel we see that very little angular momentum redistribution occurred in run H3.t12. On the other hand, in run H1.t12, bar formation leads to an excess of low angular momentum particles. At the same time, a second smaller peak forms at $2.1 \lesssim j_z \lesssim 2.6$ (see also Pfenniger & Friedli 1991). The right panel plots the location of particles in this angular momentum range. We find that the bulk of these particles occur inside the break radius, supporting the interpretation that breaks occur because of angular momentum redistribution.

6.2. The Edge-on View

Observationally, breaks have often been sought in edge-on systems, since this orientation leads to higher surface brightnesses.

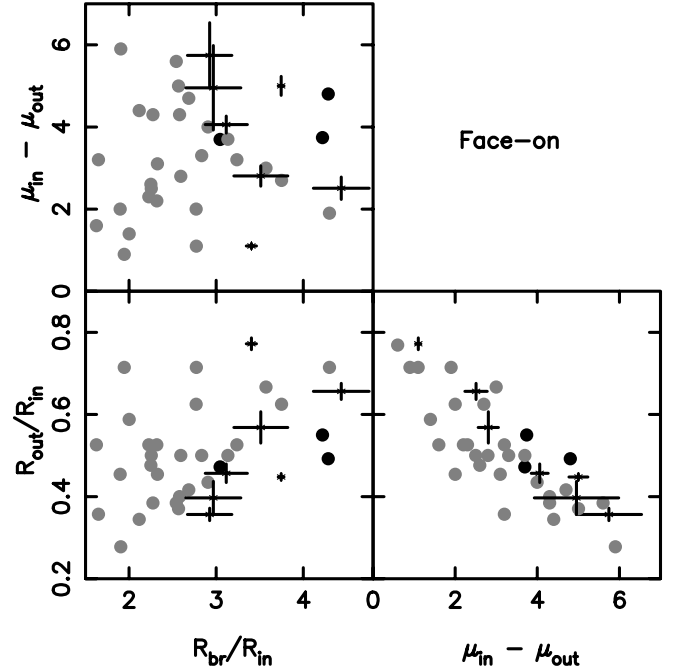


FIG. 15.—Profile break parameters for our simulations seen face-on. The filled black circles are data from Pohlen et al. (2002), and the filled gray circles are data from Pohlen & Trujillo (2006). The simulation error bars reflect temporal fluctuations; only simulations that develop breaks are plotted.

Comparing to such data is complicated by the fact that these projections integrate along the entire line of sight. At very large radii, the density profile does not evolve and reflects initial conditions. In order to avoid being biased by these effects, we again limit our double exponential fits to *projected* radii $R' < 8$; however, we integrate along the entire line of sight since to do otherwise would require an arbitrary cutoff. In order to increase the signal-to-noise ratio of our measurements, we use all particles regardless of their height above or below the disk midplane. Moreover, in the edge-on case, the break parameters depend on the bar viewing orientation. Therefore, to compare with simulations, we consider all orientations of the bar between $0^\circ \leq \phi_{\text{bar}} \leq 90^\circ$. The right panel of Figure 13 shows an example of one of our fitted edge-on breaks.

The largest observational sample of disk breaks consists of 37 edge-on galaxies studied by Pohlen (2002). We compared our simulations to these data; the results are shown in Figure 17. Variations in ϕ_{bar} lead to large variations in the parameters of the double exponential fit. Nonetheless, these fall within the range of observed systems. This is particularly striking in the $(\mu_{0,\text{in}} - \mu_{0,\text{out}}, R_{\text{out}}/R_{\text{in}})$ -plane, where the observational data span a narrow part of the space. Thus, we conclude that simple secular evolution suffices to produce realistic disk breaks.

Figure 17 shows the effect of the line-of-sight integration: runs L2.t8 (*gray asterisks*) and L2.t12 (*cyan asterisks*), which have very similar intrinsic (i.e., face-on) breaks (Fig. 14), have very different breaks in the edge-on view. Nevertheless, in both cases the resulting parameters are in good agreement with those in real galaxies.

6.3. Unbroken Profiles

Not all disk galaxies exhibit breaks (Weiner et al. 2001; Pohlen & Trujillo 2006). A successful theory of break formation must also be able to explain such unbroken profiles, which may present difficulties for a star formation threshold explanation of

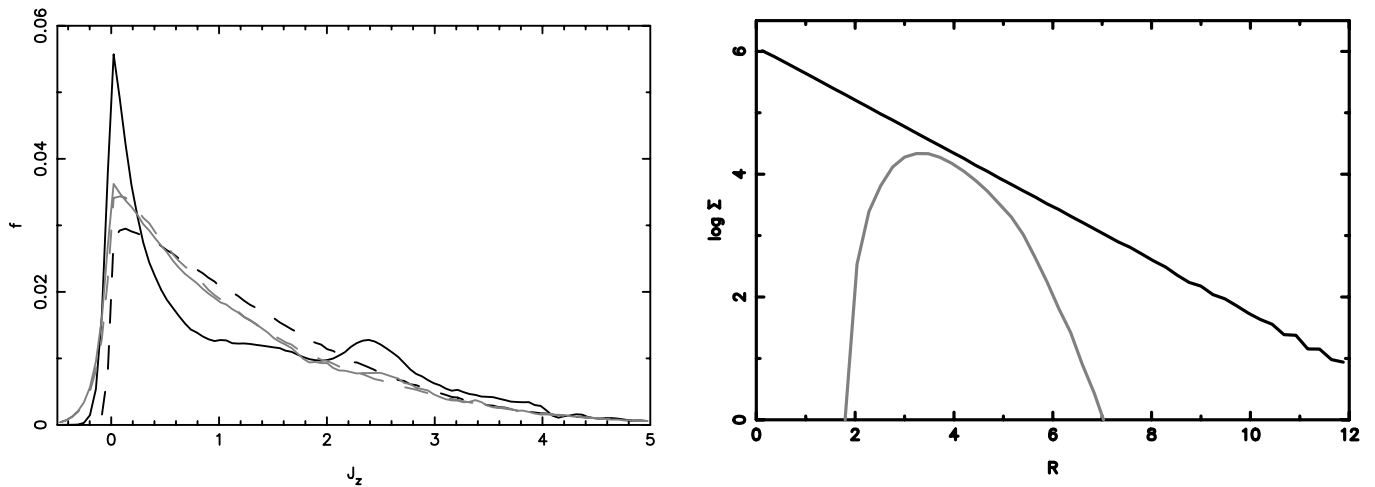


FIG. 16.—*Left:* Initial (*dashed lines*) and final (*solid lines*) distribution of angular momenta in runs H1.t12 (*black lines*) and H3.t12 (*gray lines*). *Right:* Full initial surface density (*black line*) and final surface density of particles with $2.1 \leq j_z \leq 2.6$ (*gray line*) in run H1.t12.

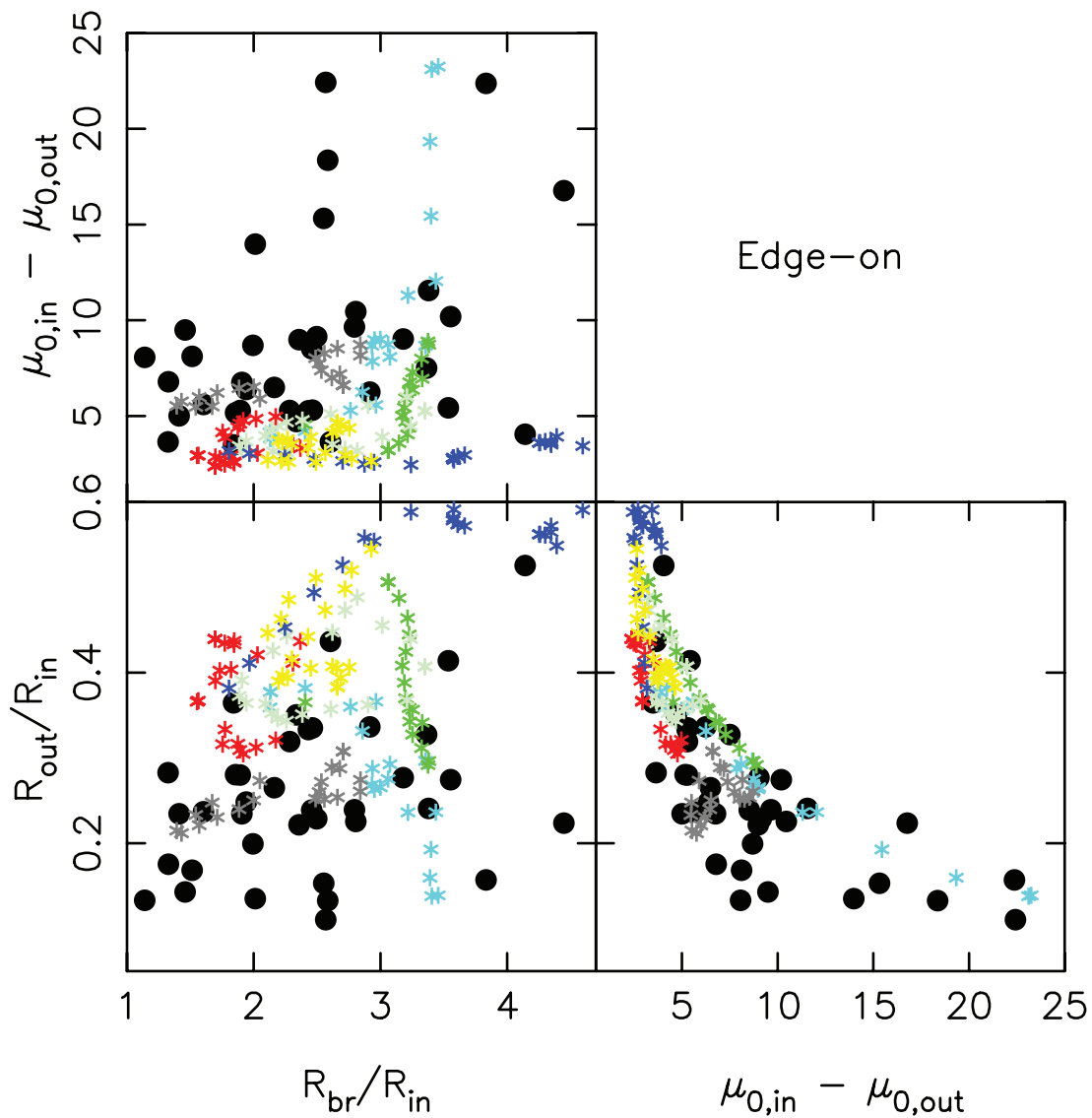


FIG. 17.—Profile break parameters for edge-on systems. The filled circles are data from Pohlen (2002). The break parameters are from runs L2.t12 (*cyan*), L2.t8 (*gray*), L4.t12 (*green*), T1.t12 (*red*), H2.t12 (*blue*), and H1.t12 (*yellow*), with varying bar position angle also shown.

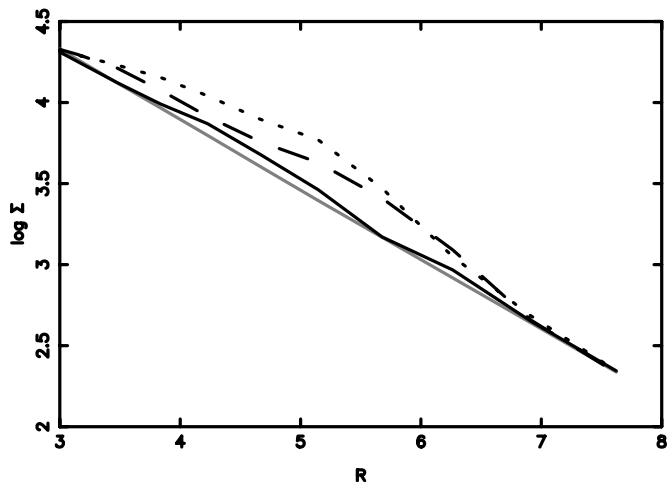


FIG. 18.—Azimuthally averaged surface density in simulations H1.t12, H2.t12, and H3.t12, in which only Q of the initial conditions is varied: run H1.t12 with $Q = 1.2$ (dotted line), run H2.t12 with $Q = 1.6$ (dashed line), and run H3.t12 with $Q = 2.0$ (solid black line). The solid gray line shows the initial profile of all three simulations.

disk breaks (Schaye 2004; Elmegreen & Hunter 2006). In our simulations, the formation of a bar is not always accompanied by the formation of a break in the disk density profile. For example, run H3.t12 formed a bar, which was not weak, but the profile remained largely exponential, as can be seen in Figure 18. Similarly, model L5.t12, with $Q = 1.6$, failed to produce a break.

We investigate the dependence of break parameters on the disk temperature by considering a set of models in which only Q of the initial conditions varies (H1.t12, H2.t12, and H3.t12). We plot the density profiles in Figure 18. At $Q = 1.2$, a prominent break develops in the density profile. At $Q = 1.6$, a break is still evident, although weaker. By $Q = 2.0$ no break forms in the density profile.

6.4. Interpretation: Bar-Spiral Coupling

The breaks that develop in our simulations are associated with the angular momentum redistribution induced by the bar. In all cases the breaks are well outside the bar semimajor axis (always

$\lesssim 3R_d$). The radius at which the breaks develop instead appears to be set by spirals resonantly coupled to the bar. Resonant couplings between bars and spirals have been described before (e.g., Tagger et al. 1987; Sygnet et al. 1988; Masset & Tagger 1997; Rautiainen & Salo 1999).

Evidence for this hypothesis from run L2.t12 is presented in Figure 19. The right panel shows the frequency spectrum of $m = 2$ perturbations. The bar's pattern speed is $\Omega_p \simeq 0.29$, while that of the spirals is $\Omega_p \simeq 0.18$. For the rotation curve of this system, this puts the corotation radius of the bar at about the inner 4 : 1 resonance radius of the spirals. The outer Lindblad resonance (OLR) of these spirals is at $R \simeq 7.5R_d$. The break sets in at $R \simeq 6R_d$, suggesting that it develops interior to the spiral OLR, at which spiral waves are absorbed. The left panel shows that the peak amplitude of $m = 2$ perturbations decreases dramatically between $7R_d \leq R \leq 9R_d$, just outside where the break develops (see Fig. 14). We stress that other spirals with different pattern speeds can and do propagate to even larger radii. Resonantly coupled spirals are favored in that they are stronger, so they transmit more efficiently the angular momentum shed by the bar during its formation.

For an independent test of this hypothesis we evolved a model with very different resonance radii: in simulation T1.t12 we forced a smaller bar with a larger pattern speed by making the disk more massive in the center (while still exponential in the outer parts). Assuming a corotation 4 : 1 bar-spiral coupling, this would bring in the spiral OLR to roughly $4.8R_d$; indeed we found a break at $R_{br} \simeq 4.5R_d$.

Thus, we propose that profile breaks develop interior to where the angular momentum shed by the bar and carried away by resonantly coupled spirals is deposited.

7. BULGE+DISK DECOMPOSITIONS

We compare the simulations with observations of bulges using the parameters of one-dimensional bulge+disk decompositions and $V_p/\bar{\sigma}$ at a given flattening. Here V_p is the peak line-of-sight velocity within some same radial range on the disk major axis and $\bar{\sigma}$ is the line-of-sight velocity dispersion (averaged within the same radial range).

We decomposed the face-on, azimuthally averaged radial mass profiles of our simulations into a central Sérsic and an outer

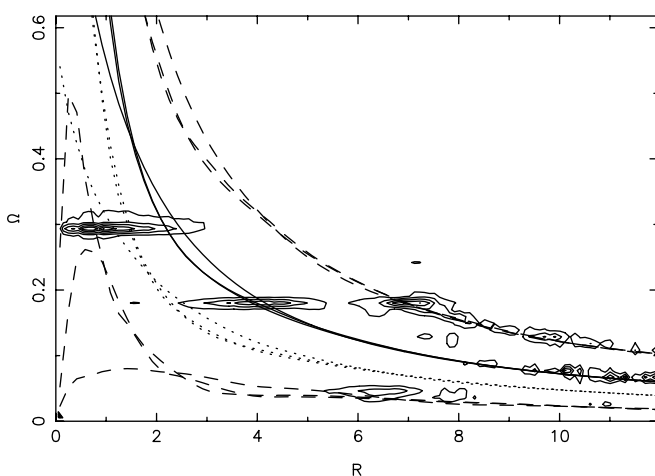
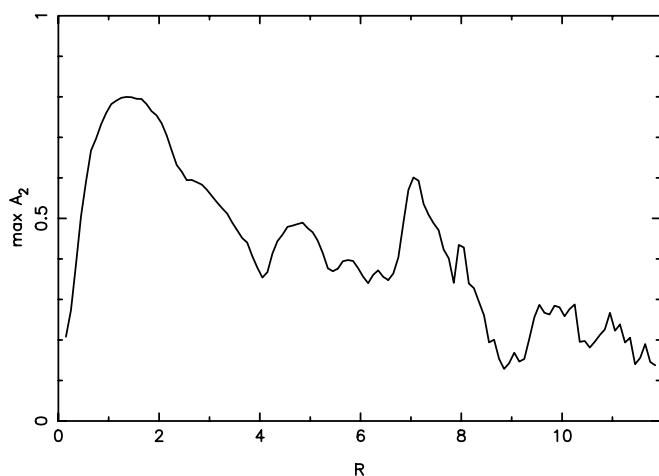


FIG. 19.—*Left*: The $m = 2$ Fourier peak amplitude of the surface density in model L2.t12. Note the abrupt drop in amplitude at $7R_d \leq R \leq 9R_d$. *Right*: Frequencies in run L2.t12. The solid lines show $\Omega(R)$, the frequency of circular rotation. The dashed lines show $\Omega - \kappa/2$ (lower) and $\Omega + \kappa/2$ (upper), while the dotted lines show $\Omega - \kappa/4$. These four sets of lines are plotted at $t = 0, 1.24, \text{ and } 4.96$ Gyr (end of the simulation). The bar forms at $t \simeq 0.62$ Gyr. Contours of the power spectrum are overplotted; these show the bar ($\Omega_p \simeq 0.29$) and spirals ($\Omega_p \simeq 0.18$). This spiral structure appears to be resonantly coupled to the bar; its OLR is close to where the break develops in the density profile.

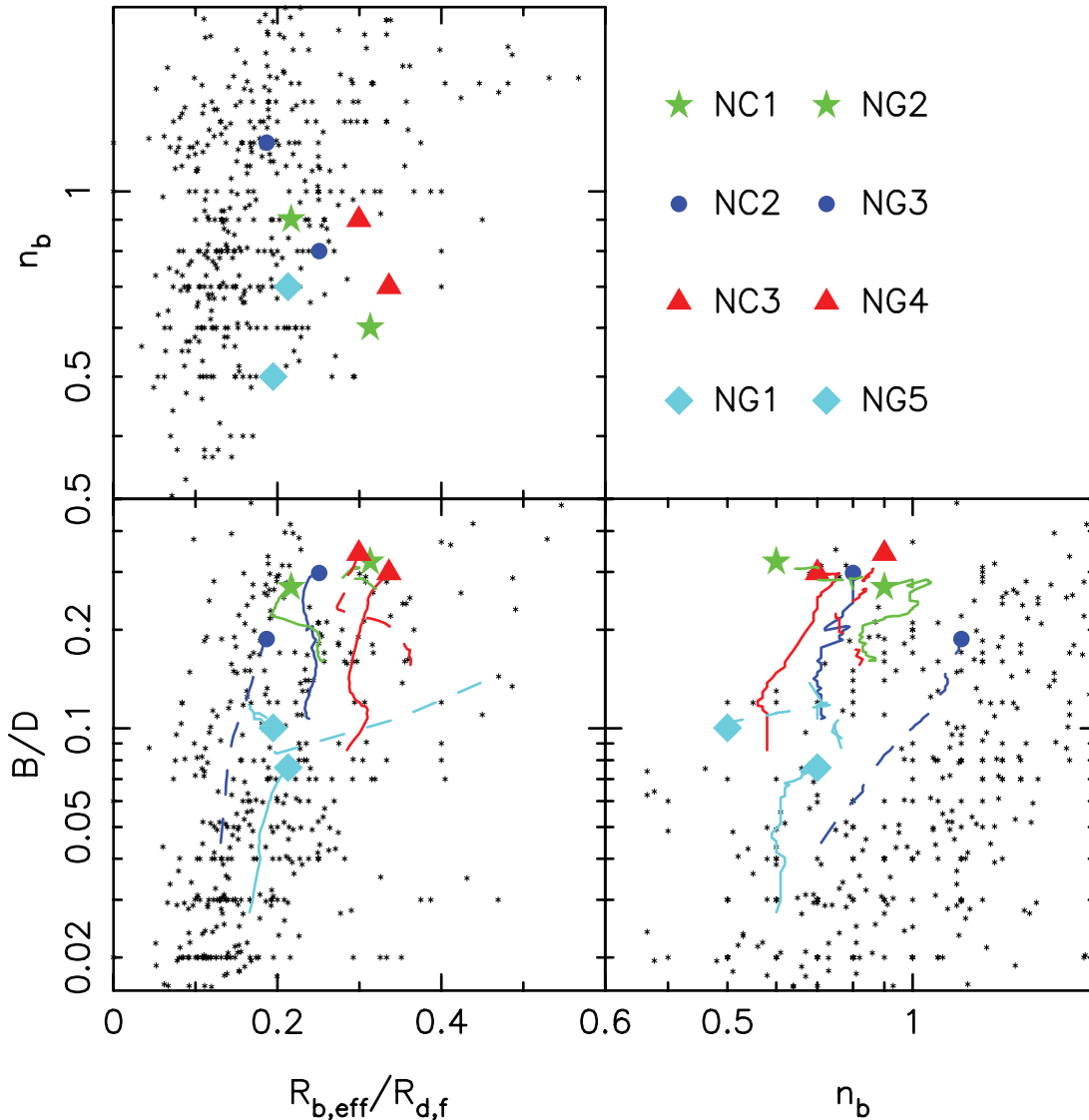


FIG. 20.— Structural parameters of the live-halo runs. In the $(B/D, R_{b,\text{eff}}/R_{d,f})$ - and $(B/D, n_b)$ -planes, the tracks indicate the evolution of each simulation *after* the bar forms. The solid lines refer to runs NC1–NC3 and NG1, while the dashed lines refer to runs NG2–NG5. We do not indicate tracks in the top left panel because these are dominated by scatter; the different simulations in this panel can be distinguished by comparing the ordering of $R_{b,\text{eff}}/R_{d,f}$ in the bottom left panel.

exponential component, which we will refer to as “bulge” and “disk,” respectively. These decompositions are characterized by five parameters: $\Sigma_{0,d}$, $\Sigma_{0,b}$ (the exponential and Sérsic central surface density, respectively), $R_{d,f}$ (final exponential scale length), $R_{b,\text{eff}}$ (the Sérsic effective radius), and n_b (the index of the Sérsic profile). In our bulge+disk fitting, we computed the fits at fixed n_b and obtained the best fit, including n_b , by repeating the fits for n_b in the range 0.1–4 in steps of 0.1, then selecting the fit with the smallest χ^2 . We did not distinguish between Freeman types in our bulge-disk decompositions. In several cases, therefore, the profile fits represent a best-fitting *average* between small and large radii.

We compare our simulations with observed galaxies in the dimensionless space spanned by the parameters $R_{b,\text{eff}}/R_{d,f}$, n_b , and B/D , the bulge-to-disk mass ratios for profiles extrapolated to infinity. The photometric data came from two separate studies. Our first sample comes from MacArthur et al. (2003), who presented bulge+disk decompositions for a sample of 121 predominantly late-type galaxies of various inclinations, observed in B , V , R , and H bands. This study considered only systems with

Freeman type I (i.e., exponential) disk profiles in all bands. As our systems often exhibited transient type II phases, we also used the decompositions of Graham (2001, 2003). These were obtained from the diameter-limited sample of 86 low-inclination disk galaxies of all Hubble types observed in the B , R , I , and K bands by de Jong & van der Kruit (1994). It is well known that bulge+disk structural parameters depend on the filter used (e.g., Möllenhoff 2004). We compared directly with the data in all passbands; thus, any discrepancies we find between simulations and observations are not likely to be due to any differences in mass-to-light ratios of disks and bulges.

Paper I presented the decompositions of the rigid-halo models where we showed that the models partly overlap with the observations but are mismatched elsewhere. This mismatch can be diminished if only those bulges rounder than the disk are considered, but at the cost of requiring inclinations $i \gtrsim 60^\circ$. In Figure 20 we present the face-on bulge+disk decompositions for live-halo models after bar formation. Several trends are worth noting. Compared with Paper I, the main changes are the generally smaller n_b and B/D values, as well as the smaller discrepancy with

observations, although a small discrepancy is still evident in the $(B/D, n_b)$ -plane. All simulations fall in the same space as observed galaxies in the $(B/D, R_{b, \text{eff}}/R_{d, f})$ -plane. In the absence of gas, the values of B/D tend to their largest values. Moreover, this quantity increases with time, a result of the continuing loss of disk angular momentum to the halo, leading to denser disk centers. Indeed, we find that the density of the inner region increases through most of the simulation. Introducing 10% gas leads to a lower B/D when the gas can cool (NG1) because the resulting central gas concentration leads to a weaker bar. When the gas is adiabatic (NG2), the central mass that grows is significantly smaller, the bar amplitude is not much different from the collisionless case, and the B/D ratio is about as large as in the collisionless systems. When star formation is included (NG3), the B/D ratio is intermediate between NG1 and NG2 and is continually increasing, changing by almost an order of magnitude as gas is turned into stars. When gas accounts for 50% of the disk mass, the B/D ratio is again high when gas is adiabatic (NG4) but remains smaller when it can cool (NG5), in which case a bulge is built via the clump instability (Noguchi 1999; Immeli et al. 2004).

Some overall trends can be noticed. Generally the systems evolve parallel to the mean observed correlation between B/D and $R_{b, \text{eff}}/R_{d, f}$ largely because n_b does not evolve much. In the $(n_b, R_{b, \text{eff}}/R_{d, f})$ - and $(B/D, n_b)$ -planes, the simulations show a slight tendency to fall outside the observed range, with B/D evolving toward values larger than observed. The exception is model NG3, which evolves parallel to the mean relation between these two parameters. This model is also comfortably within the range of observed bulges in the $(B/D, R_{b, \text{eff}}/R_{d, f})$ -plane. Thus, dissipation with star formation is an important ingredient in the secular assembly of the bulges seen today.

We compared the kinematics of the bulges with observations in the $(V/\sigma, \epsilon)$ -plane at various orientations. Because of the smaller number of particles compared with the rigid-halo simulations, we were not able to fit ellipses as in Paper I. We therefore obtained the effective radius of the inclined system through a Sérsic bulge+exponential disk fit to the mass distribution along the major (i.e., inclination) axis. As in Paper I, because our bulges are poorly fitted by a de Vaucouleurs profile, we measure kinematic quantities and mean ellipticities at both one-half and one effective radius and use the differences as an error estimate. Ellipticities were measured from the two-dimensional mass moments of the projected mass distribution at these two radii, with the difference between the two giving an error estimate. Each of the final states of the simulations is viewed at inclination of $i = 30^\circ$ or 60° and for position angles $\phi_b = 0^\circ, 45^\circ, \text{ or } 90^\circ$.

In Figure 21 we report the results. The larger scatter in the live-halo simulations compared with the rigid-halo simulations (shown in Paper I) is mainly due to the lower number of particles and related discreteness noise of the mass distribution at radii only a few times larger than the softening length. Overall live and rigid-halo simulations occupy very similar locations, with many systems below the locus of oblate isotropic systems flattened by rotation. Indeed, the simulations include systems significantly flatter than the observations. These are usually systems in which the peanut is less pronounced due to weak buckling and the bar still very strong (a clear example is run NG3), and they are viewed at small position angles and high inclinations; these objects would appear markedly barlike and thus probably would not be included in surveys of bulges. Anisotropy clearly plays a role in determining the flattening, which is unsurprising given that almost all bars survive. Systems with gas tend to have higher V/σ for a given value of the ellipticity, and the most gas-rich systems are those that lie closest to the locus of oblate isotropic rotators.

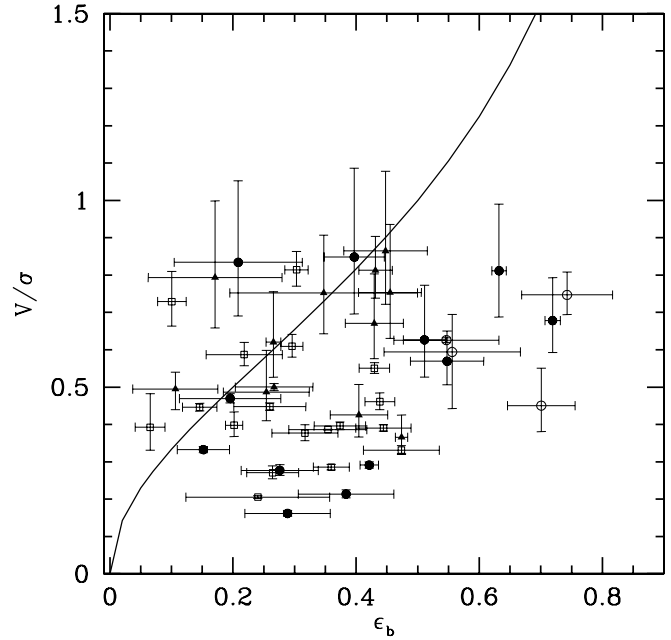


FIG. 21.—Kinematic properties of the live-halo simulations. Open squares are for collisionless runs, filled circles are for runs with adiabatic gas, filled triangles are for runs with gas and radiative cooling, and open circles are for the star formation run. Each run was viewed with different inclinations and position angles. Error bars are estimated as described in the text.

This is expected if the gas falling toward the center sheds a fraction of its angular momentum to the stars and spins them up. Run NG3 produces a system with the highest flattening due to a combination of a strong bar and the suppression of the buckling of the bar.

7.1. The Pseudobulge Formed by the Clump Instability

The gas sinking to the center of run NG5 was sufficient to destroy the bar. Because we have no star formation in this simulation, we are left with a rotationally supported massive central gas disk. Star formation would have presumably led to a thin, rotationally supported pseudobulge. The mass of gas within one $R_{b, \text{eff}} = 0.83$ kpc (which is measured face-on from only the stellar component) is $1.2 \times 10^{10} M_\odot$. The associated aperture dispersion within $R_{b, \text{eff}}$ is $\sigma = 141 \text{ km s}^{-1}$. In order for the resulting bulge to sit on the M_\bullet - σ relation (Gebhardt et al. 2000; Ferrarese & Merritt 2000; Tremaine et al. 2002), less than 0.3% of this gas needs to collapse into a black hole. This shows that disk instabilities are another way, in addition to gas-rich mergers (Kazantzidis et al. 2005), by which a significant reservoir of gas can be built to feed an already existing central supermassive black hole or perhaps produce a new one. Since violent gravitational instabilities in the gas disk need a high gas mass fraction, such a mechanism might have played a role in the formation of seed black holes at high redshift.

8. DISCUSSION AND CONCLUSIONS

In this paper we explored the secular evolution of disk structural parameters using simulations. The initial galaxy model is similar to a “Milky Way”-type galaxy that might form within a Λ CDM universe. We have found that bar formation leads to a significant mass redistribution both in and away from the disk plane. The evolution of stellar surface density profiles and the formation of peanut-shaped, dynamically hot stellar structures in the central regions of the disk are both consequences of bar formation. Angular momentum redistribution can lead to large

changes in density profiles, resulting in profiles that can be reasonably fitted by a central Sérsic and an outer exponential component. These can be identified as bulge and disk components, respectively, although fundamentally they remain bars. On purely photometric grounds it is difficult to distinguish these profiles from bulge+disk decompositions for real galaxies; however, kinematically these secular bulges clearly fall below the oblate isotropic rotators. Real bulges are observed to be at or above this line.

We have shown that when bars occur in a typical bright spiral galaxy, they are difficult to destroy. The buckling instability, which is one way a peanut-shaped bulge can form, is suppressed when gas is highly concentrated in the center of the disk. A peanut can form other than through a major buckling event in such systems. It is interesting to note that when buckling occurs, it peaks typically ~ 2 Gyr after the bar forms. It is only at this point that the peanut-shaped bulge appears.

Our main results can be summarized as follows:

1. While strong buckling always leads to significant vertical heating, we found that heating does not always result in a peanut structure. When buckling occurs, the central density may increase; in one simulation this increase more than doubled the central density. As a consequence, the Sérsic index of the resulting bulge+disk decomposition increases somewhat.

2. The effect of gas on the buckling instability depends on the gas physics. When the gas evolution included radiative cooling, buckling was not possible and no peanuts formed. When the gas is adiabatic, buckling can occur and peanuts form. This difference might arise because the higher central gas concentration suppresses bending modes, as suggested by the correlation between strength of buckling and central gas mass concentration. However, a clear test is needed to discriminate between this scenario and one in which buckling does not occur because the energy in the modes is dissipated by radiative cooling. Peanuts can still be recognized by the negative minimum in the s_4 criterion (Paper II) even when gas is present because it sinks to small radii, with the peanut at larger radii.

3. We found no case in which buckling destroyed a bar. In Paper I we demonstrated this with the rigid-halo simulations. In this paper we showed that this result continues to hold when a live halo is included. The most damaging buckling events we saw were induced in the rigid-halo simulations by slowing bars, but even in those cases a bar survived. Sometimes, however, the surviving bar is weak and may be better described as SAB rather than SB.

4. Density profiles may evolve substantially under the action of a bar. Reasonable bulge+disk decompositions can be fitted to the resulting profiles. When comparing the fits with observed galaxies, purely collisionless secular evolution gives rise to systems marginally consistent with bulges in nature. The presence of a modest (10%) amount of gas produces systems that are better able to match observations. Star formation helps further and leads to an evolution of structural parameters parallel to their locus for observed galaxies. Secular evolution generally gives rise to nearly exponential inner profiles. Kinematically, however, the central bulgelike components of our simulations clearly fall below the locus of oblate isotropic rotators (at or above which real bulges occur in nature), reflecting the fact that they are still, fundamentally, bars.

5. The amount of evolution of a density profile following bar formation depends sensitively on the Toomre Q of the initial disk. When this is small, the inner disk needs to shed a large amount of angular momentum to form a bar and the central den-

sity steepens considerably. When the disk is hotter, the density change is smaller. As a result, the exponential scale length of the disk outside the bar region depends on the initial disk kinematics. Thus, a distribution of dark matter halo specific angular momenta cannot trivially be related to a distribution of disk scale lengths, as is often assumed.

6. Angular momentum redistribution also leads to realistic breaks in the surface density of disks. The radius at which breaks occur is interior to the outer Lindblad resonance of spirals resonantly coupled to the bar. When the initial disk is hot, little angular momentum redistribution occurs and no density breaks occur; thus, secular evolution can also account for galaxies that do not exhibit any breaks. The breaks that result in these simulations are in very good agreement with observations, including not only the break radii in units of inner disk scale length but also outer scale lengths and the difference between central surface brightnesses of the two exponentials. On the other hand, we cannot exclude that angular momentum redistribution driven by other than bars does not account for some or most of the observed breaks. In particular, spirals excited by interactions may constitute another channel by which such breaks may form; the presence of breaks in unbarred galaxies may require such a mechanism. Since our disk break formation simulations were all collisionless, we cannot address whether star formation thresholds play any role in break formation, but two results here suggest that these may not play a prominent role. First, we are able to produce disks without truncations, which models invoking star formation thresholds may have difficulty in producing. Secondly, it is clear that the breaks that do form in our simulations are quite insensitive to extent of the initial disks. The ease with which angular momentum redistribution gives rise to realistic profile breaks, together with the ability to produce also profiles without breaks, provides strong incentives for exploring such models further. Moreover, the type of angular momentum exchange we are advocating here as leading to breaks need not be necessarily driven by bars, and external perturbations can also play a role. In that case, depending on the frequency of the perturbation, antitruncations (Erwin et al. 2005) may also be possible in a unified picture.

The fraction of disks with bars is $\sim 30\%$ at both low (Sellwood & Wilkinson 1993) and high (Jogee et al. 2004) redshift, and this increases to $\sim 70\%$ at low redshift when measured via dust-penetrating infrared observations (Knapen 1999; Eskridge et al. 2000). Since, as we show, bars are long lived, we are forced to the conclusion that disk galaxies know at an early epoch whether or not they will form a bar and there is simply little room for continued bar formation as a function of cosmic time. Thus, secular evolution has had a long time to act on galaxies.

The results of this paper demonstrate a strong coupling between the properties and evolution of disk galaxies and their associated inner and outer morphological and structural parameters. In contrast, semianalytic models of disk structural parameters that invoke specific angular momentum conservation miss the important effects of bar formation on disk structure. As noted in Paper I, a more nuanced analysis that takes into account secular evolution may help to alleviate discrepancies between predictions for disk galaxy structure from cosmological models (e.g., Mo et al. 1998) and observations (de Jong & Lacey 2000).

Nonetheless, secular evolution cannot account for all discrepancies between theory and observation. An example is the difficulty cosmological models have in forming bulgeless disks as extended as those observed (D’Onghia & Burkert 2004). The N -body simulations of D’Onghia & Burkert (2004) showed that halos with a quiet merging history since $z = 3$ (which are

expected to lead to bulgeless disks, but see also Springel & Hernquist 2005) have a median $\lambda \simeq 0.023$ with a scatter $\sigma_{\ln \lambda} \simeq 0.3$. On the other hand, van den Bosch et al. (2001) measured their observed mean at $\lambda \simeq 0.067$. Thus, the mean of λ in the cosmological simulations is more than 3σ smaller than observed. Our simulations indicate that the fraction of galaxies that form pure exponential disks must be higher (and extends to higher mass galaxies such as our own Milky Way) before secular evolution turns them into more disk+bulge-like systems. However, even if all of these systems would have lower λ -values, the distribution of λ -values of quiet merger halos makes it unlikely that secular evolution can account for the discrepancy between predictions and observations. An interesting test of Λ CDM will be

whether enough halos with quiet merger histories form to account for a higher fraction of bulgeless galaxies.

Discussions with Stéphane Courteau, Aaron Dutton, Peter Erwin, Lauren MacArthur, Michael Pohlen, Juntao Shen, and especially Frank van den Bosch were useful. Thanks also to Michael Pohlen for sharing his data with us in advance of publication. T. Q. and V. P. D. acknowledge partial support from NSF ITR grant PHY-0205413. We thank the anonymous referee for a very careful reading and a detailed report that helped improve this paper.

REFERENCES

- Abadi, M. G., Navarro, J. F., Steinmetz, M., & Eke, V. R. 2003, *ApJ*, 591, 499
 Andredakis, Y. C., & Sanders, R. H. 1994, *MNRAS*, 267, 283
 Araki, S. 1985, Ph.D. thesis, MIT
 Athanassoula, E., & Bureau, M. 1999, *ApJ*, 522, 699
 Balsara, D. S. 1995, *J. Comput. Phys.*, 121, 357
 Bate, M. R., & Burkert, A. 1997, *MNRAS*, 288, 1060
 Baugh, C. M., Cole, S., & Frenk, C. S. 1996, *MNRAS*, 283, 1361
 Benson, A. J., Bower, R. G., Frenk, C. S., Lacey, C. G., Baugh, C. M., & Cole, S. 2003, *ApJ*, 599, 38
 Berentzen, I., Heller, C. H., Shlosman, I., & Fricke, K. J. 1998, *MNRAS*, 300, 49
 Binney, J., & Tremaine, S. 1987, *Galactic Dynamics* (Princeton: Princeton Univ. Press)
 Birnboim, Y., & Dekel, A. 2003, *MNRAS*, 345, 349
 Bournaud, F., Combes, F., & Semelin, B. 2005, *MNRAS*, 364, L18
 Bullock, J. S., Dekel, A., Kolatt, T. S., Kravtsov, A. V., Klypin, A. A., Porciani, C., & Primack, J. R. 2001, *ApJ*, 555, 240
 Bureau, M., & Athanassoula, E. 1999, *ApJ*, 522, 686
 Bureau, M., & Freeman, K. C. 1999, *AJ*, 118, 126
 Carollo, C. M. 1999, *ApJ*, 523, 566
 Carollo, C. M., Stiavelli, M., de Zeeuw, P. T., & Mack, J. 1997, *AJ*, 114, 2366
 Carollo, C. M., Stiavelli, M., de Zeeuw, P. T., Seigar, M., & Dejonghe, H. 2001, *ApJ*, 546, 216
 Carollo, C. M., Stiavelli, M., & Mack, J. 1998, *AJ*, 116, 68
 Carollo, C. M., Stiavelli, M., Seigar, M., de Zeeuw, P. T., & Dejonghe, H. 2002, *AJ*, 123, 159
 Cole, S., Aragon-Salamanca, A., Frenk, C. S., Navarro, J. F., & Zepf, S. E. 1994, *MNRAS*, 271, 781
 Cole, S., Lacey, C. G., Baugh, C. M., & Frenk, C. S. 2000, *MNRAS*, 319, 168
 Combes, F., Debbasch, F., Friedli, D., & Pfenniger, D. 1990, *A&A*, 233, 82
 Combes, F., & Sanders, R. H. 1981, *A&A*, 96, 164
 Courteau, S., de Jong, R. S., & Broeils, A. H. 1996, *ApJ*, 457, L73
 Dalcanton, J. J., Spergel, D. N., & Summers, F. J. 1997, *ApJ*, 482, 659
 Debattista, V. P., Carollo, C. M., Mayer, L., & Moore, B. 2004, *ApJ*, 604, L93 (Paper I)
 ———. 2005, *ApJ*, 628, 678 (Paper II)
 Debattista, V. P., & Sellwood, J. A. 1998, *ApJ*, 493, L5
 ———. 2000, *ApJ*, 543, 704
 de Grijs, R., Kregel, M., & Wesson, K. H. 2001, *MNRAS*, 324, 1074
 de Jong, R. S. 1996, *A&A*, 313, 45
 de Jong, R. S., & Lacey, C. 2000, *ApJ*, 545, 781
 de Jong, R. S., & van der Kruit, P. C. 1994, *A&AS*, 106, 451
 D'Onghia, E., & Burkert, A. 2004, *ApJ*, 612, L13
 Elmegreen, B. G., & Hunter, D. A. 2006, *ApJ*, 636, 712
 Erwin, P., Beckman, J. E., & Pohlen, M. 2005, *ApJ*, 626, L81
 Eskridge, P. B., et al. 2000, *AJ*, 119, 536
 Fall, S. M., & Efstathiou, G. 1980, *MNRAS*, 193, 189
 Ferguson, A. M. N., Irwin, M. J., Ibata, R. A., Lewis, G. F., & Tanvir, N. R. 2002, *AJ*, 124, 1452
 Ferrarese, L., & Merritt, D. 2000, *ApJ*, 539, L9
 Firmani, C., & Avila-Reese, V. 2000, *MNRAS*, 315, 457
 Gardner, J. P. 2001, *ApJ*, 557, 616
 Gebhardt, K., et al. 2000, *ApJ*, 539, L13
 Gerhard, O. E. 1993, *MNRAS*, 265, 213
 Governato, F., et al. 2004, *ApJ*, 607, 688
 Graham, A. W. 2001, *AJ*, 121, 820
 ———. 2003, *AJ*, 125, 3398
 Hatton, S., Devriendt, J. E. G., Ninin, S., Bouchet, F. R., Guiderdoni, B., & Vibert, D. 2003, *MNRAS*, 343, 75
 Helmi, A., White, S. D. M., de Zeeuw, P. T., & Zhao, H.-S. 1999, *Nature*, 402, 53
 Hernquist, L. 1993, *ApJS*, 86, 389
 Hohl, F. 1971, *ApJ*, 168, 343
 Ibata, R. A., Gilmore, G., & Irwin, M. J. 1994, *Nature*, 370, 194
 Immeli, A., Samland, M., Gerhard, O., & Westera, P. 2004, *A&A*, 413, 547
 Jimenez, R., Verde, L., & Oh, S. P. 2003, *MNRAS*, 339, 243
 Jog, C., & Solomon, P. M. 1991, in *IAU Symp. 146, Dynamics of Galaxies and Their Molecular Cloud Distributions*, ed. F. Combes & F. Casoli (Dordrecht: Kluwer), 277
 Jogee, S., et al. 2004, *ApJ*, 615, L105
 Katz, N. 1992, *ApJ*, 391, 502
 Katz, N., & Gunn, J. E. 1991, *ApJ*, 377, 365
 Katz, N., Kereš, D., Davé, R., & Weinberg, D. H. 2003, in *The IGM/Galaxy Connection: The Distribution of Baryons at $z = 0$* , ed. J. L. Rosenberg & M. E. Putman (Dordrecht: Kluwer), 185
 Kauffmann, G., White, S. D. M., & Guiderdoni, B. 1993, *MNRAS*, 264, 201
 Kazantzidis, S., et al. 2005, *ApJ*, 623, L67
 Kereš, D., Katz, N., Weinberg, D. H., & Davé, R. 2005, *MNRAS*, 363, 2
 Klypin, A., Zhao, H.-S., & Somerville, R. S. 2002, *ApJ*, 573, 597
 Knapen, J. H. 1999, in *ASP Conf. Ser. 187, The Evolution of Galaxies on Cosmological Timescales*, ed. J. E. Beckman, & T. J. Mahoney (San Francisco: ASP), 72
 Kormendy, J. 1993, in *IAU Symp. 153, Galactic Bulges*, ed. H. Dejonghe & H. J. Habing (Dordrecht: Kluwer), 209
 Kormendy, J., Bender, R., & Bower, G. 2002, in *ASP Conf. Ser. 273, The Dynamics, Structure and History of Galaxies*, ed. G. S. Da Costa & H. Jerjen (San Francisco: ASP), 29
 Kuijken, K., & Merrifield, M. R. 1995, *ApJ*, 443, L13
 Lilly, S., et al. 1998, *ApJ*, 500, 75
 Lütticke, R., Dettmar, R.-J., & Pohlen, M. 2000, *A&AS*, 145, 405
 MacArthur, L. A., Courteau, S., & Holtzman, J. A. 2003, *ApJ*, 582, 689
 Martin, C. L., & Kennicutt, R. C., Jr. 2001, *ApJ*, 555, 301
 Martinez-Valpuesta, I., & Shlosman, I. 2004, *ApJ*, 613, L29
 Martinez-Valpuesta, I., Shlosman, I., & Heller, C. 2006, *ApJ*, 637, 214
 Masset, F., & Tagger, M. 1997, *A&A*, 322, 442
 Mayer, L., & Wadsley, J. 2004, *MNRAS*, 347, 277
 McMillan, P. J., & Dehnen, W. 2005, *MNRAS*, 363, 1205
 Merritt, D., & Sellwood, J. A. 1994, *ApJ*, 425, 551
 Mo, H. J., Mao, S., & White, S. D. M. 1998, *MNRAS*, 295, 319
 Möllenhoff, C. 2004, *A&A*, 415, 63
 Navarro, J. F., Frenk, C. S., & White, S. D. M. 1996, *ApJ*, 462, 563
 Navarro, J. F., & Steinmetz, M. 2000, *ApJ*, 538, 477
 Noguchi, M. 1999, *ApJ*, 514, 77
 Peletier, R. F., & Balcells, M. 1996, *AJ*, 111, 2238
 Pérez, I. 2004, *A&A*, 427, L17
 Pfenniger, D. 1984, *A&A*, 134, 373
 Pfenniger, D., & Friedli, D. 1991, *A&A*, 252, 75
 Pohlen, M. 2002, Ph.D. thesis, Ruhr-Univ. Bochum
 Pohlen, M., Dettmar, R.-J., Lütticke, R., & Aronica, G. 2002, *A&A*, 392, 807
 Pohlen, M., & Trujillo, I. 2006, *A&A*, submitted (astro-ph/0603682)
 Quillen, A. C. 2002, *AJ*, 124, 722
 Rafikov, R. R. 2001, *MNRAS*, 323, 445
 Raha, N. 1992, Ph.D. thesis, Univ. Manchester
 Raha, N., Sellwood, J. A., James, R. A., & Kahn, F. D. 1991, *Nature*, 352, 411
 Rautiainen, P., & Salo, H. 1999, *A&A*, 348, 737
 Schaye, J. 2004, *ApJ*, 609, 667
 Sellwood, J. A., & Debattista, V. P. 2006, *ApJ*, 639, 868
 Sellwood, J. A., & Valluri, M. 1997, *MNRAS*, 287, 124
 Sellwood, J. A., & Wilkinson, A. 1993, *Rep. Prog. Phys.*, 56, 173
 Sérsic, J. L. 1968, *Atlas de Galaxias Australes* (Córdoba: Obs. Astron.)

- Shen, J., & Sellwood, J. A. 2004, *ApJ*, 604, 614
- Somerville, R. S., & Primack, J. R. 1999, *MNRAS*, 310, 1087
- Sommer-Larsen, J., Götz, M., & Portinari, L. 2003, *ApJ*, 596, 47
- Sotnikova, N. Ya., & Rodionov, S. A. 2003, *Astron. Lett.*, 29, 321
- . 2005, *Astron. Lett.*, 31, 15
- Spergel, D. N., et al. 2003, *ApJS*, 148, 175
- Springel, V., & Hernquist, L. 2005, *ApJ*, 622, L9
- Springel, V., & White, S. D. M. 1999, *MNRAS*, 307, 162
- Stadel, J. G. 2001, Ph.D. thesis, Univ. Washington
- Steinmetz, M., & Navarro, J. F. 2002, *NewA*, 7, 155
- Stinson, G., Seth, A., Katz, N., Wadsley, J., Governato, F., & Quinn, T. 2006, *MNRAS*, submitted (astro-ph/0602350)
- Sygnnet, J. F., Tagger, M., Athanassoula, E., & Pellat, R. 1988, *MNRAS*, 232, 733
- Tagger, M., Sygnnet, J. F., Athanassoula, E., & Pellat, R. 1987, *ApJ*, 318, L43
- Terndrup, D. M., Davies, R. L., Frogel, J. A., DePoy, D. L., & Wells, L. A. 1994, *ApJ*, 432, 518
- Toomre, A. 1964, *ApJ*, 139, 1217
- . 1981, in *Structure and Evolution of Normal Galaxies*, ed. S. M. Fall & D. Lynden-Bell (Cambridge: Cambridge Univ. Press), 111
- Tremaine, S., et al. 2002, *ApJ*, 574, 740
- Trujillo, I., & Pohlen, M. 2005, *ApJ*, 630, L17
- van den Bosch, F. C. 1998, *ApJ*, 507, 601
- . 2000, *ApJ*, 530, 177
- . 2001, *MNRAS*, 327, 1334
- . 2002, *MNRAS*, 332, 456
- van den Bosch, F. C., Abel, T., Croft, R. A. C., Hernquist, L., & White, S. D. M. 2002, *ApJ*, 576, 21
- van den Bosch, F. C., Burkert, A., & Swater, R. A. 2001, *MNRAS*, 326, 1205
- van der Kruit, P. C. 1979, *A&AS*, 38, 15
- van der Kruit, P. C., & Searle, L. 1981a, *A&A*, 95, 105
- . 1981b, *A&A*, 95, 116
- van der Marel, R. P., & Franx, M. 1993, *ApJ*, 407, 525
- Wadsley, J. W., Stadel, J., & Quinn, T. 2004, *NewA*, 9, 137
- Weinberg, M. D. 1985, *MNRAS*, 213, 451
- Weiner, B. J., Williams, T. B., van Gorkom, J. H., & Sellwood, J. A. 2001, *ApJ*, 546, 916
- White, S. D. M., & Rees, M. J. 1978, *MNRAS*, 183, 341